THE SUBARU/*XMM-NEWTON* DEEP SURVEY (SXDS). III. X-RAY DATA

YOSHIHIRO UEDA,[1] MICHAEL G. WATSON,[2] IAN M. STEWART,[2,3] MASAYUKI AKIYAMA,[4,5] AXEL D. SCHWOPE,[6]
GEORG LAMER,[6] JACOBO EBRERO,[7] FRANCISCO J. CARRERA,[7] KAZUHIRO SEKIGUCHI,[8] TOHRU YAMADA,[5]
CHRIS SIMPSON,[9] GÜNTHER HASINGER,[10] AND SILVIA MATEOS[2]

ABSTRACT

We present the X-ray source catalog in the Subaru/*XMM-Newton* deep survey. A continuous area of 1.14 deg² centered at R.A. = 02^h18^m and decl. = $-05°$ is mapped by seven pointings with *XMM-Newton* covering the 0.2–10 keV band. From the combined images of the EPIC pn and MOS cameras, we detect 866, 1114, 645, and 136 sources with sensitivity limits of 6×10^{-16}, 8×10^{-16}, 3×10^{-15}, and 5×10^{-15} ergs cm^{-2} s^{-1} in the 0.5–2, 0.5–4.5, 2–10, and 4.5–10 keV bands, respectively, with detection likelihood ≥ 7 (corresponding to a confidence level of 99.91%). The catalog consists of 1245 sources in total including 32 extended-source candidates. The averaged log N–log S relations are in good agreement with previous results, bridging the flux range between *Chandra* deep surveys and brighter surveys. The log N–log S relations show significant spatial variation among pointings on a scale of 0.2 deg². Analyzing the autocorrelation function, we detect significant clustering signals from the 0.5–2 keV band sample, which can be fit with a power-law form $(\theta/\theta_c)^{-0.8}$ with a correlation length of $\theta_c = 5.9^{+1.0}_{-0.9}$ arcsec when the integral constraint term is included. In the 2–10 keV band, however, the clustering is not significant with a 90% upper limit of $\theta_c < 1.5''$.

Subject headings: catalogs — diffuse radiation — galaxies: active — X-rays: galaxies — X-rays: general

Online material: color figures, machine-readable table

1. INTRODUCTION

The Subaru/*XMM-Newton* Deep Survey (SXDS; K. Sekiguchi et al. 2008, in preparation) is, along with COSMOS (Scoville et al. 2007; Hasinger et al. 2007), one of the largest multiwavelength survey projects with an unprecedented combination of depth and sky area over a contiguous region of >1 deg². The main aims of the SXDS are to make an accurate measurement of the global properties of the universe without being affected by cosmic variance and to reveal the evolution of the large-scale structure. The SXDS consists of a wealth of multiwavelength data taken by the most modern observing facilities: X-ray imaging/spectroscopic data in the 0.2–10 keV band taken by the European Photon Imaging Camera (EPIC; Strüder et al. 2001; Turner et al. 2001) on board *XMM-Newton* (Jansen et al. 2001); multicolor (B, V, R, i', z') deep optical images by Suprime-Cam on the Subaru telescope (Furusawa et al. 2008); deep near-infrared maps (J, H, K) observed as the Ultra Deep Survey (UDS) in the United Kingdom Infrared Deep Sky Survey (UKIDSS; Lawrence et al. 2007), mid- and far-infrared data (3.6–160 μm) taken with *Spitzer*[11];

the submillimeter (850 μm) map by the SCUBA Half Degree Extragalactic Survey (SHADES; Mortier et al. 2005)[12]; and the deep radio image (1.4 GHz) by the Very Large Array (Simpson et al. 2006). The SXDS field is centered at R.A. = 02^h18^m and decl. = $-05°$, and the total field of the Subaru Suprime-Cam and *XMM-Newton* EPIC images covers an area of 1.3 and 1.14 deg², respectively. The overall survey design and details of each survey are summarized in K. Sekiguchi et al. (2008).

The data of *XMM-Newton* constitute a major component of the SXDS project. X-ray surveys are a powerful tool to trace the cosmological evolution of active phenomena in the universe, including active galactic nuclei (AGNs) and clusters/groups of galaxies. The main constituents of X-ray sources that make up the X-ray background (XRB) are AGNs (for a recent review, see Brandt & Hasinger 2005). Their dominant populations are "obscured" AGNs (Setti & Woltjer 1989), where the central engine is blocked by dust and/or gas in the line of sight. In particular, surveys by hard X-rays above 2 keV are the most efficient approach to detect these obscured AGN populations of various luminosity classes with least bias, thanks to their strong penetrating power against the photoelectric absorption of matter and small contamination from stars. In fact, the surface density of AGNs detected in the most sensitive X-ray surveys (Alexander et al. 2003) far exceeds that detected in the optical bands (e.g., Wolf et al. 2003), thus providing us with the most complete and clean samples for AGN studies including heavily obscured, low-luminosity ones that dominate the whole AGN populations by number.

The tight correlation between the mass of a supermassive black hole (SMBH) in the galactic center and that of the galactic bulge (Ferrarese & Meritt 2000; Gebhardt et al. 2000) indicates strong links between the growth of SMBHs and star formation in the past. Since AGNs are phenomena that mark the process of growth of SMBHs in galactic centers, to elucidate the evolution of AGNs is a fundamental issue for understanding the history of the universe. Combination of ultradeep pencil beam surveys and large

[1] Department of Astronomy, Kyoto University, Kyoto 606-8502, Japan.
[2] Department of Physics and Astronomy, University of Leicester, Leicester, LE1 7RH, UK.
[3] Jodrell Bank Centre for Astrophysics, University of Manchester, Oxford Road, Manchester, M13 9PL, UK.
[4] Subaru Telescope, National Astronomical Observatory of Japan, Hilo, HI, 96720.
[5] Astronomical Institute, Tohoku University, Sendai 980-8578, Japan.
[6] Astrophysikalisches Institut Potsdam, An der Sternwarte 16, 14482 Potsdam, Germany.
[7] Instituto de Física de Cantabria (CSIC-UC) Avda. de los Castros, 39005 Santander, Spain.
[8] National Astronomical Observatory of Japan, 2-21-1 Osawa, Mitaka, Tokyo 181-8588, Japan.
[9] Astrophysics Research Institute, Liverpool John Moores University, Twelve Quays House, Egerton Wharf, Birkenhead CH41 1LD, UK.
[10] Max-Planck-Institut für Extraterrestrische Physik, Giessenbachstrasse 85748 Garching, Germany.
[11] The *Spitzer* Legacy Survey and part of the *Spitzer* Wide-area Infrared Extragalactic (SWIRE) survey.

[12] The SXDS field is also the field of SCUBA-2 Cosmology Legacy Survey.

TABLE 1
Log of the *XMM-Newton* Observations in the SXDS Field

Field	Obs. ID	R.A.[a] (deg)	Decl.[a] (deg)	P.A.[b] (deg)	Start (UT)	End (UT)	Exposure[c] (s)
SDS-1	0112370101	34.47838	−4.98117	73.6	2000 Jul 31 22:38	Aug 01 14:04	40361
	0112371001	34.47883	−4.98050	74.5	2000 Aug 02 21:13	Aug 03 13:15	42473
SDS-2	0112370301	34.87900	−4.98047	74.8	2000 Aug 04 21:05	Aug 05 14:00	40220
SDS-3	0112370401	34.67971	−4.63422	75.7	2000 Aug 06 07:53	Aug 06 17:38	14341
	0112371501	34.67958	−4.63414	75.7	2000 Aug 06 20:58	Aug 06 23:20	4080
SDS-4	0112371701	34.27946	−4.63394	76.0	2000 Aug 08 07:57	Aug 08 15:02	21277
	0112372001	34.32404	−4.66858	245.7	2003 Jan 07 04:41	Jan 07 11:56	25940
SDS-5	0112370601	34.07854	−4.98164	76.1	2002 Aug 12 06:06	Aug 12 18:52	34377
SDS-6	0112370701	34.27754	−5.32797	74.9	2002 Aug 08 15:28	Aug 09 04:43	46802
SDS-7	0112370801	34.67792	−5.32856	74.9	2002 Aug 09 05:52	Aug 09 19:02	36803

[a] Mean pointing position (J2000.0) of the optical axis.
[b] Mean position angle.
[c] Net exposure for the pn data after screening.

area surveys have revealed the cosmological evolution of the X-ray luminosity function of AGNs (Ueda et al. 2003; La Franca et al. 2005; Barger et al. 2005; Hasinger et al. 2005). The global accretion history of the universe is similar to that of star formation (see, e.g., Franceschini et al. 1999; Marconi et al. 2004). An important finding is that the number density of more luminous AGNs have a peak at higher redshifts compared with less luminous ones. This behavior is called "downsizing" or "antihierarchical" evolution, which is opposite to a naive expectation from the standard structure formation theory of the universe. Similar trends were also obtained in the star formation history (e.g., Cowie et al. 1996; Kodama et al. 2004). These facts imply two modes of "co-evolution" of galaxies and SMBHs for different masses. It could be explained by the feedback from supernova and AGNs (e.g., Granato et al. 2004). Deep multiwavelength surveys enable us to observe various populations in different evolutionary stage, giving the best opportunities to investigate how galaxies and SMBHs co-evolved with cosmic time.

Despite this major progress on AGN evolution in recent years, there are several critical issues to be resolved by current and future X-ray surveys, even if we limit the scope only to X-ray–detected AGNs. Immediate objectives include (1) whether or how the fraction of obscured AGNs evolves with redshift, (2) the number density of Compton thick AGNs (those whose line-of-sight absorption exceeds $N_{\rm H} > 10^{24}$ cm^{-2}), (3) the evolution of the AGN luminosity function at high redshifts ($z \gtrsim 4$) to be compared with the results from optical QSO surveys, and (4) the evolution of clustering properties of AGNs as a function of luminosity and type. The SXDS X-ray survey, one of the few "wide" and "deep" surveys, will give important steps to answer these questions and to establish the average properties of the AGN populations. Population synthesis models of the XRB utilize the results from deep surveys in a limited area at the faintest flux levels (Ueda et al. 2003; Gilli et al. 2007), which would be subject to cosmic variance when we discuss the XRB spectrum with ≈10% accuracy. This is crucial when we discuss a relatively minor contribution of some X-ray sources, such as Compton thick AGNs. To constrain the statistical properties of rare objects, such as high-redshift QSOs, much larger cosmic volume is necessary than in the currently available deep surveys. By surveying a continuous area with a large depth, we can also study the evolution of the large-scale structure probed by AGNs. It helps us to understand the physical conditions that triggers AGN activity for different luminosity class, type (1 or 2), and redshift. At the flux limits of the SXDS, we can detect the most dominant populations of X-ray sources that contribute to the

XRB. In all of these studies, high completeness of identification (redshift determination) is crucial. The multiwavelength data are particularly useful in identifying X-ray sources even if optical spectroscopy is difficult for a population of "optically faint" AGNs (Alexander et al. 2001).

In this paper, we describe the X-ray data of the SXDS based on the *XMM-Newton* survey performed in 2000 and 2003. We present the whole X-ray catalog, and basic statistical properties of the detected X-ray sources. The X-ray data have been used in a number of studies in the SXDS projects, detection of ultraluminous X-ray sources in nearby galaxies (Watson et al. 2005), mid-IR and radio-selected Compton-thick AGNs (Martínez-Sansigre et al. 2007), radio sources (Simpson et al. 2006), Lyα sources (Saito et al. 2008; Ouchi et al. 2008), and optical variability selected AGNs (Morokuma et al. 2008). A series of papers on optical identification of the X-ray sources are forthcoming (M. Akiyama et al. 2008, in preparation). The paper is organized as follows. Section 2 summarizes the observation of the *XMM-Newton*. In § 3 we describe the detailed procedure of data analysis and present the source list and its statistics. Sections 4 and 5 show the results of log N–log S relations and autocorrelation functions, respectively. In § 6, long-term time variability of X-ray sources is studied in a selected field. Section 7 summarizes the conclusions. Throughout the paper, the cosmological parameters ($H_0, \Omega_m, \Omega_\lambda$) = (100 h km s^{-1} Mpc^{-1}, 0.3, 0.7) are adopted.

2. OBSERVATIONS

The SXDS field, centered at R.A. = $02^{\rm h}18^{\rm m}$ and decl. = $-05°$, was mapped with *XMM-Newton* in the 0.2–10 keV band by seven pointings, one deep (nominal exposure 100 ks) observation in the center surrounded by six shallower (50 ks each) ones. *XMM-Newton* carries three EPICs, pn, MOS1, and MOS2, each has a field of view (FOV) of about $30' \times 30'$. The pointing positions are arranged so that the combined X-ray map, having a "flower petal" pattern, covers essentially the whole region of the optical images taken with the Subaru telescope, mosaic of five Suprime-Cam images in each band (Furusawa et al. 2008). There are small overlapped regions between these pointings, making the X-ray image continuous without gaps over an area of about 1.14 deg^2, although the sensitivity is not completely uniform over the entire map due to different exposures and instrumental effects, such as vignetting (see § 4.1 for details).

Table 1 gives the observation log, including the pointing position, observation time, and net exposure obtained after screening out high background time. We designate the pointings as SDS-1

for the central field and SDS-2 through SDS-7 for the surrounding ones in a clockwise direction. The observations were performed in three discrete epochs, the first from 2000 July 31 to August 8 (for SDS-1, 2, 3, 4), the second from 2002 August 8 to 12 (for SDS-5, 6, 7), and the third on 2003 January 7 to supplement the unfulfilled exposure of SDS-4. The observation of each pointing were performed continuously except for short intervals (several hours) in SDS-1 and SDS-3 and a long interval (2.5 yr) in SDS-4. The "thin" filters were used for the three cameras in all the observations.

3. ANALYSIS

3.1. Image Production

The reduction of the EPIC data was performed by using the Science Analysis System (SAS) software. We used SAS version 6.1.0[13] for image creation and all the subsequent analysis, while an earlier version of SAS (that very similar to version 5.3.3) was utilized to produce the event files from which we start the image analysis, processed in the *XMM-Newton* Survey Science Center (SSC) Pipeline Processing System (PPS) facility in University of Leicester.

As the first step, we created sky images with a bin size of $4''$ in four energy bands, 0.3–0.5, 0.5–2, 2–4.5, and 4.5–10 keV, separately for each observation ID and detector. The 7.9–8.3 keV band was excluded to avoid the instrumental background of Cu K-lines (Strüder et al. 2001). With the standard event selection, we accumulated good photon events with "patterns" of 0 through 12 (MOS1 and MOS2) or 0 through 4 (pn). The time region of background flare was excluded by examining the light curve. This leaves a net exposure of about 60%–80% of the allocated observing time, as listed in Table 1.

To achieve the best positional accuracy, we corrected the absolute astrometry of the EPIC image of each obsID with respect to the Subaru *R*-band image in the following way. We performed source detection from each observation, and cross-correlated the obtained (tentative) source list with the optical catalog (Furusawa et al. 2008) to calculate the mean positional offsets. Then we corrected the original images for these offsets, which were found to be $0''$–$1.3''$, consistent with the estimated error in the absolute astrometry of *XMM-Newton*. This correction also minimizes systematic errors caused by summing up multiple observations for the case of SDS-1, 3, and 4.

3.2. Source Detection

We produce source lists separately from different pointings (SDS-1 through 7). Later, these are merged into one list by excluding overlapping regions to define a statistically independent sample from the whole data (§ 3.3). The overall flow of the source detection is similar to the one adopted in the SSC PPS used to produce the 2XMM catalog (Watson et al. 2008), although several improvements are employed here. The main differences are as follows: (1) we perform source detection to the summed image of pn, MOS1, and MOS2, not to individual ones; (2) we optimize several parameters of the spline interpolation in making background maps; (3) special care is paid to separate neighboring sources.

3.2.1. Background Maps

For each observation, energy band, and detector, we create a background map from the image by spline interpolation with the SAS program `esplinemap` after excluding sources found with `eboxdetect`, which perform simple source detection based on a cell detection algorithm. After optimization of parameters, we verify that the obtained models well represent the profiles of the background (i.e., the unresolved XRB plus non X-ray background) over the whole FOV without large deviation from the data.

3.2.2. Summation of Images

We sum up the pn, MOS1, MOS2 images and background maps for each energy band and each "pointing," which means also combining those of multiple observations for SDS-1, 3, and 4. This enables us to achieve the best sensitivity from the whole available data in the simplest manner. At the same time, we can avoid technical problems in the position and flux determination that would be caused by image gaps between CCD chips in a single detector.

To obtain exposure maps, we first calculated them for each instrument in narrow energy bands of every 0.5 keV, using the SAS task `eexpmap`. Then we took their count-rate–weighted average, normalized to the pn count rate in a given survey band. The count rate distribution is calculated through the energy response of each instrument assuming a power-law photon index of 1.5 above 2 keV and 2.0 below 2 keV. The dependence on assumed photon indices is negligibly small in the analysis. The cross-calibration of effective area between the pn and MOS cameras is known to be accurate within 5% level, and its uncertainty does not affect the results.

With this procedure, we are able to treat the summed images and exposure maps as if they were created from a single pn detector regardless of the detected position. In the following analysis, we present the flux of a source in terms of a "pn-equivalent" count rate. Strictly speaking, this treatment may not be perfectly accurate in the image fitting process described below, because the positions of the optical axis in the combined image are not common for different detectors and observations, which could affect a precise modeling of the combined point-spread function (PSF) of the mirrors. To estimate *maximum* systematic errors caused by this effect, we make the same analysis by changing the position of the optical axis to that of a MOS camera. We find that the fluxes of sources obtained in the two analyses match each other by 1.3% level, confirming that this approximation is justified at this accuracy.

Figure 1 shows the pseudo–three-colored X-ray image of the SXDS field combined from the seven pointings. This image is made by the `export` command in the IRAF package.[14] As the inputs, we use the exposure-corrected, background-subtracted pn+MOS1+MOS2 images in the 0.5–2, 2–4.5, and 4.5–10 keV bands, corresponding to red, green, and blue colors, respectively. They are smoothed by a Gaussian profile with a 1 σ width of $4''$ over the entire field. Larger color fluctuation is apparently seen in outer regions compared with the central region due to the shorter exposure.

3.2.3. Maximum Likelihood Fit

The source list from each pointing is obtained by the maximum likelihood fit applied to the detector co-added images in the four energy bands by using the SAS task `emldetect`. The `emldetect` program reads images, background maps, and exposure maps in a single or multiple energy bands and makes a simultaneous fit to

---

[13] The latest current calibration files (CCF) as of 2005 January 31 were used.

[14] IRAF is distributed by the National Optical Astronomy Observatory, which is operated by the Association of Universities for Research in Astronomy, Inc., under cooperative agreement with the National Science Foundation.
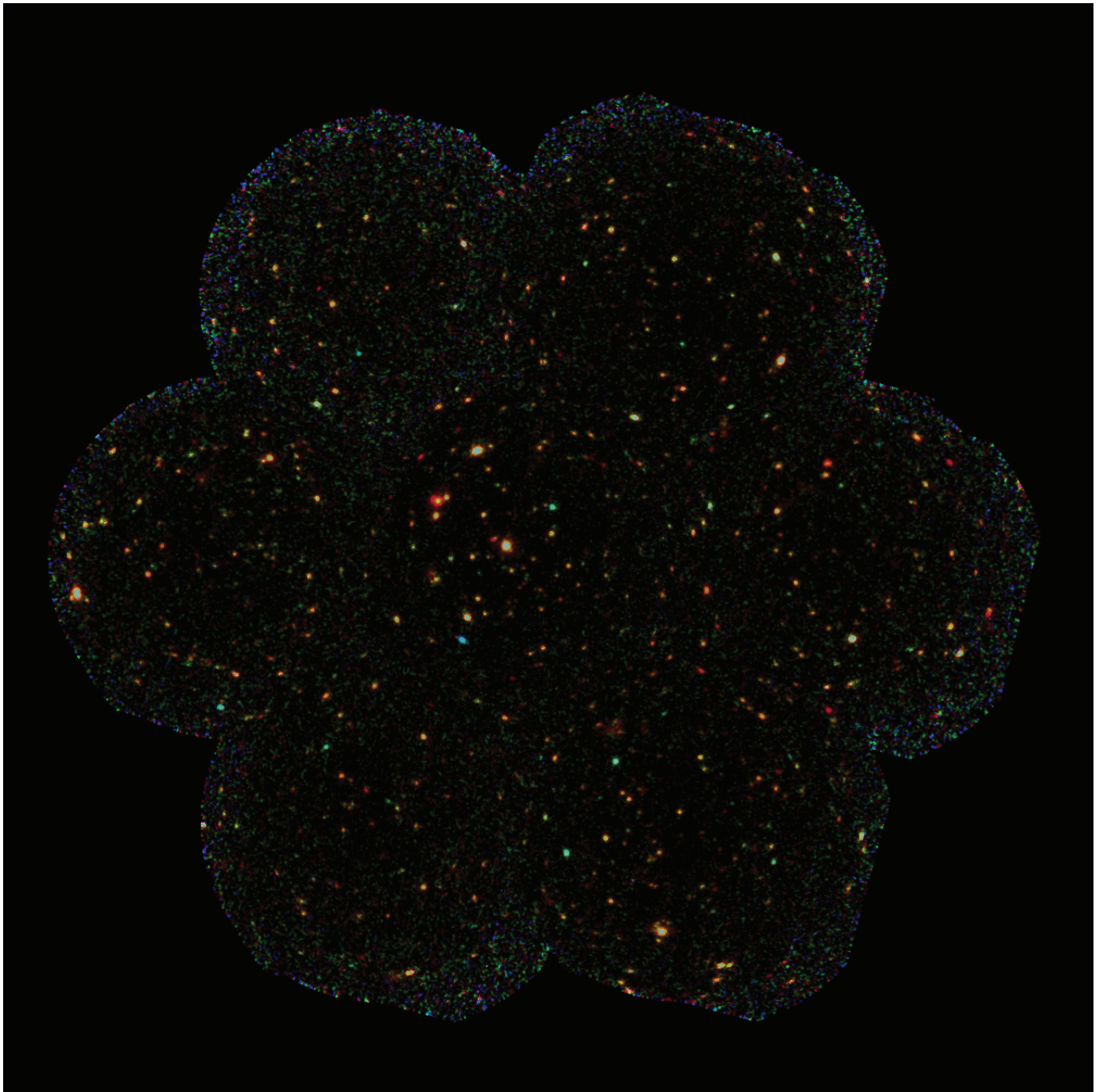
FIG. 1.—Smoothed, three-colored X-ray image of the whole SXDS field obtained from the energy bands of 0.5–2 keV (*red*), 2–4.5 keV (*green*), and 4.5–10 keV (*blue*).

the images with a model consisting of PSFs over the background map, based on the input list of source candidates. It returns the fitted position, vignetting-corrected count rate, and detection likelihood (hereafter called "ML," for maximum likelihood) of each source. The obtained count rate corresponds to the total flux in the entire PSF.

To make the list complete, this process is iterated twice in the following manner. We first perform cell detection by `eboxdetect` with a cell size of $20'' \times 20''$ to obtain a list of source candidates with minimum likelihood of 3.2, which is used as an input to the first run of `emldetect`. In both programs we allow the flux and position of a source to be free parameters. We find that in some

cases the above cell size is too large to completely detect sources in a high-density region. To supplement this, we also perform cell-detection with a $12'' \times 12''$ cell size and add new source candidates detected with high significance into the source list obtained above. In this stage, by human inspection, we pay attention not to include obviously fake sources such as a part of a PSF tail from nearby bright sources, diffuse emission, and false detection close to gaps between CCD chips. The merged list is again input to `emldetect`, producing a final source list.

Through the fitting process, we find that there are sources that are likely to be confused by the PSF of neighboring ones in crowded regions. To measure the fluxes of these sources with the

TABLE 2
THE X-RAY SOURCE LIST OF THE SXDS

XMM	R.A. (deg)	Dec. (deg)	Error	0.3–0.5	0.5–2	2–4.5	4.5–10	0.5–4.5	2–10	0.3–0.5	0.5–2	2–4.5	4.5–10	HR1	HR2	HR3	Field[a]	Offset[b]	Exp.[c]	Bgd.[d]	Note[e]
					Likelihood					Count Rate (counts ks⁻¹)				Hardness Ratio							
0001.......	33.85387	−4.92870	2.36	0.0	19.9	3.2	0.4	26.5	5.1	0.00 ± 0.09	3.45 ± 0.79	1.39 ± 0.63	0.86 ± 0.81	1.00 ± 0.05	−0.42 ± 0.21	−0.24 ± 0.49	5	15.6	9.6	2.6	
0002.......	33.85392	−4.90221	2.24	16.1	33.7	2.5	0.8	37.1	6.2	2.69 ± 0.74	6.33 ± 1.25	1.38 ± 0.72	1.18 ± 0.90	0.40 ± 0.14	−0.64 ± 0.16	−0.08 ± 0.46	5	16.0	5.5	2.6	
0003.......	33.86346	−5.03354	2.88	0.3	0.0	0.0	6.8	0.4	7.5	0.24 ± 0.27	0.18 ± 0.31	0.09 ± 0.25	2.72 ± 0.82	−0.13 ± 1.01	−0.33 ± 1.43	0.94 ± 0.17	5	14.8	12.2	2.6	
0004.......	33.87124	−4.96292	2.99	5.2	14.1	0.0	0.0	11.1	0.0	0.79 ± 0.34	2.33 ± 0.57	0.00 ± 0.11	0.00 ± 0.28	0.49 ± 0.19	−1.00 ± 0.09	. . .	5	14.2	15.5	2.6	
0005.......	33.87257	−4.89099	1.85	2.5	11.8	6.7	0.7	22.4	8.6	0.68 ± 0.38	2.85 ± 0.73	1.76 ± 0.55	0.88 ± 0.69	0.61 ± 0.19	−0.24 ± 0.19	−0.33 ± 0.38	5	15.2	9.7	2.6	
0006.......	33.87878	−4.98760	2.84	0.0	2.6	2.9	0.0	8.7	2.8	0.00 ± 0.04	0.89 ± 0.41	0.61 ± 0.29	0.00 ± 0.38	1.00 ± 0.10	−0.19 ± 0.32	−1.00 ± 1.24	5	13.6	17.9	2.5	
0007.......	33.89418	−5.06675	0.56	131.3	554.7	5.5	0.0	484.2	4.3	6.86 ± 0.88	25.08 ± 1.56	1.20 ± 0.43	0.03 ± 0.25	0.57 ± 0.05	−0.91 ± 0.03	−0.94 ± 0.40	5	13.6	14.1	2.8	
0008.......	33.90476	−4.94904	1.25	24.9	41.6	6.7	0.0	50.9	5.9	1.56 ± 0.33	3.57 ± 0.56	0.85 ± 0.27	0.00 ± 0.21	0.39 ± 0.11	−0.62 ± 0.11	−0.99 ± 0.49	5	12.3	16.8	2.2	
0009.......	33.90754	−5.08932	2.64	0.0	6.8	3.4	0.0	13.6	3.0	0.00 ± 0.06	1.75 ± 0.56	0.77 ± 0.34	0.14 ± 0.32	1.00 ± 0.06	−0.39 ± 0.23	−0.69 ± 0.61	5	13.4	17.3	2.7	
0010.......	33.91171	−5.01450	1.30	10.6	72.1	6.0	2.3	75.5	11.0	0.89 ± 0.25	4.53 ± 0.59	0.73 ± 0.25	0.90 ± 0.44	0.67 ± 0.09	−0.72 ± 0.09	0.11 ± 0.29	5	11.8	17.4	2.2	

NOTE.—Table 2 is available in its entirety in the electronic edition of the *Astrophysical Journal Supplement*. A portion is shown here for guidance regarding its form and content.

[a] The pointing ID (1–7) where the source is detected.

[b] The offset angle in units of arcminutes from the mean optical axis in the corresponding pointing.

[c] The total pn-equivalent exposure (sum of pn, MOS1, and MOS2) at the source position in units of ks, corrected for the vignetting in the 0.5−4.5 keV band.

[d] The background rate in the 0.5−4.5 keV band at the source position in units of 10^{-3} counts ks⁻¹ arcsec⁻².

[e] Set to be "C" if multiple-source fitting was performed to obtain the fluxes to take into account possible source confusion with nearby sources (see § 3.2.3).

best accuracy, we perform an image fit in each region by allowing the positions and fluxes of the multiple sources (up to three) to vary simultaneously in order to solve the coupling of the fluxes self-consistently. Their angular separation is typically $12''$–$24''$. Their fluxes are replaced with the new values obtained here, and the ML values are calculated for each source at the fixed position. The number of pairs of such possibly confused sources are about 10 per pointing and are marked by flag "C" in the last column of the source catalog (Table 2).

The statistic that `emldetect` uses to fit the source parameters is the C statistic defined by Cash (1979). For a Poissonian probability distribution, appropriate to the measurement of X-ray events by *XMM-Newton*, Cash's statistic takes the form

$$C = 2 \sum_{i=1}^{N} \sum_{j=1}^{M} (e_{i,j} - n_{i,j} \ln e_{i,j}) + \text{constant},$$

where $e_{i,j}$ is the expected number of X-ray events in the ith pixel and jth energy band, $n_{i,j}$ is the detected number of events in that pixel/band, and the sum is over N pixels within the detection region and the M energy bands used (here $=4$ as stated). The value of $e_{i,j}$ is obtained by adding the value of the source model at that pixel/band to the expected contribution from the background; $e_{i,j}$ is thus a function of the source model parameters.

After arriving at those values of the source parameters that minimize C, the detection likelihood (formally, the probability of the null hypothesis) for those optimum values is then calculated. Cash's prescription for this is to form the difference,

$$\Delta C = C_{\text{null}} - C_{\text{best}},$$

where C_{null} is C calculated by setting the amplitude of the source model to zero and C_{best} is the minimum result returned by the fitting routine. According to Cash's theory, ΔC is distributed approximately as χ^2 for ν degrees of freedom, where ν is the number of fitted parameters. The probability $p(\chi^2 \geq \Delta C)$ of obtaining the calculated value of ΔC or greater by chance fluctuations of the detected background can therefore be obtained in terms of the complementary incomplete gamma function Q as follows:

$$p(\chi^2 \geq \Delta C) = Q(\nu/2, \ \Delta C/2).$$

The value of ML is set within `emldetect` to equal $-\ln(p)$. Note that the statistics must be treated with caution when the total number of photon counts used for the fit are very small ($\lesssim 9$), which is not the case in our analysis.

The ML value as calculated in the above way is viewed as more sensitive than the simple box-detection statistic used by `eboxdetect`, because it uses information about the source PSF to help reject random fluctuations of the detected background. Offsetting this is a possible bias introduced by the fact that `emldetect` is not given "free rein" over the whole field but is applied only to a small number of restricted areas of the field, at locations of candidate sources already found by `eboxdetect`. If the detection threshold of `eboxdetect` is set to too high a value, there is a risk that a real source with a good shape, but not many counts, will be missed by the combined detection process. In order to avoid this bias, one ought therefore to run the preceding `eboxdetect` with a detection threshold set deliberately low. On the other hand, since `emldetect` must go through the computationally intensive fitting process with each of its candidates, it will be impractical to provide it with too long a list of candidates. The respective values

TABLE 3
THE LIST OF CANDIDATES OF EXTENDED SOURCES IN THE SXDS

Number	Extent Likelihood	Extent[a] (arcsec)
0034............	5.1	2.8 ± 0.5
0051............	11.4	17.9 ± 1.2
0140............	6.8	22.0 ± 3.3
0153............	9.2	4.7 ± 0.4
0156............	7.4	4.2 ± 0.9
0239............	4.4	3.9 ± 1.0
0280............	4.5	19.3 ± 3.3
0285............	36.6	16.0 ± 1.8
0287............	4.9	4.8 ± 1.3
0292............	5.5	4.1 ± 1.3
0396............	4.0	5.9 ± 1.8
0441............	12.4	12.7 ± 1.4
0453............	7.2	12.4 ± 2.2
0514............	30.9	21.0 ± 2.0
0552............	6.5	7.1 ± 1.4
0621............	6.5	6.6 ± 1.4
0622............	4.3	4.6 ± 1.4
0625............	5.7	2.9 ± 1.8
0646............	9.1	3.5 ± 0.8
0647............	10.3	9.4 ± 1.6
0712............	6.6	4.3 ± 0.8
0784............	14.3	33.6 ± 3.3
0796............	20.5	3.0 ± 0.3
0829............	48.6	11.5 ± 0.6
0852............	4.7	3.3 ± 0.2
0876............	19.6	17.4 ± 1.6
0889............	5.7	17.2 ± 3.1
0934............	10.0	4.7 ± 0.4
1152............	5.0	11.8 ± 3.9
1168............	4.6	18.4 ± 2.8
1169............	5.2	3.7 ± 1.1
1176............	31.4	15.3 ± 1.1

[a] The source extent when a Gaussian profile is adopted ($1\ \sigma$).

of 3.2 and 7 adopted here for the `eboxdetect` and `emldetect` likelihood cutoffs were chosen with this necessary compromise in mind.

An additional advantage of using `emldetect` to determine the final source parameters is its ability to add the models of already fitted sources to an internal background map. Since the sources are processed in the order of their brightness, it is possible to take into account the background introduced by bright sources when fitting the fainter sources.

3.2.4. *Examining Source Extent*

Up to this stage, all sources are assumed to be pointlike. To constrain the spatial extent of the detected sources, we perform an image fit by allowing the source extent to be a free parameter assuming a Gaussian profile. The source positions are fixed at the input ones. This procedure yields a list of extended source candidates from the SXDS field (Table 3). For these sources, the fluxes listed in Table 2 correspond to those obtained in this process with consideration of the source extent. However, as our procedure is essentially dedicated to detection of pointlike sources in the earlier stage, this list must be regarded to be incomplete. A more extensive approach to search for extended sources will be presented elsewhere (A. Finoguenov et al. 2008, in preparation).

3.3. *Source List*

Thus, we obtain seven source lists separately from different pointings (SDS-1 through 7), containing the information of

TABLE 4
NUMBER OF DETECTED SOURCES

Detection Band	0.3−0.5	0.5−2	2−4.5	4.5−10	0.5−4.5	2−10	One Band Only[a]
0.3−0.5 keV	**357**	339	235	73	341	253	16
0.5−2 keV		**866**	412	113	853	466	13
2−4.5 keV			**487**	121	474	461	4
4.5−10 keV				**136**	125	133	3
0.5−4.5 keV.....................					**1114**	550	169
2−10 keV.........................						**645**	78

NOTE.—Number of sources commonly detected in the combination of two bands (or a single band, in boldface) are listed.
[a] Number of sources detected only in one band given in the first column.

position and fluxes with the ML values in the four energy bands, 0.3−0.5, 0.5−2, 2−4.5, and 4.5−10 keV. In these tentative lists, we keep all sources whose summed ML from the four bands is equal to or exceeds 5, which will be further screened in the following way.

To make scientific research in comparison with previous studies, it is quite useful to define a sample selected in standard bands such as 0.5−4.5 keV (XID band) and 2−10 keV band (hard band). Although the combined flux and ML can be calculated from those in the two individual bands (i.e., 0.5−2 and 2−4.5 keV for the XID band and 2−4.5 and 4.5−10 keV for the hard band), its statistical treatment would become quite complex; for instance, the sensitivity limit cannot be uniquely determined as a function of ML at a given position, depending on the source spectrum. Hence, to obtain a well-defined sample selected in the XID or hard band in the same way as in the four narrow bands, we calculate their ML values by repeating the likelihood fit using the 0.5−4.5 or 2−10 keV image with the background map summed from the two narrow bands. In the fit, the positions of the sources are fixed,[15] and no new sources are considered.

In this paper we adopt a threshold for the detection likelihood of 7 in a single band. Thus, from the tentative source lists, we se-

[15] Since we fix the position in the XID and hard bands, the corresponding ΔC value is smaller than those obtained in the four individual bands for a given ML, because the degree of freedom ν is reduced by 2. This is also the case for the "confused" sources whose ML values are obtained by fixing the position (see § 3.2.3). We properly take these effects into account in the analysis of log N–log S relations and autocorrelation function.

lect only those detected with ML $\geq$ 7 either in the 0.3−0.5 keV (ultrasoft), 0.5−2 keV (soft), 2−4.5 keV (medium), 4.5−10 keV (ultrahard), 0.5−4.5 keV (XID), or 2−10 keV (hard) band, to be included in the final list. Further, for statistical analysis using this sample, it is convenient to have a single source list merged from the seven pointings; as mentioned above, there are overlapping regions between different pointings in the outer edge of the FOV, where same sources are repeatedly detected. To exclude such duplication, we only refer to the results of a single pointing that achieves the highest sensitivity at a given position, based on sensitivity maps in the XID band (see below).

Table 2 gives the source list in the SXDS field complied in this way, sorted by right ascension and declination: (col. [1]) source number; (cols. [2] and [3]) the X-ray source position as determined by *XMM-Newton* (R.A. and decl.); (col. [4]) the statistical error in the position estimated through the maximum likelihood fit (root sum square of the 1 σ error in each direction); (cols. [5]–[10]) the ML value in each energy band; (cols. [11]–[14]) the vignetting-corrected count rate in each energy band; (cols. [15]–[17]) the hardness ratios defined as HR1 = $(S - US)/(S + US)$, HR2 = $(M - S)/(M + S)$, HR3 = $(UH - M)/(UH + M)$, where US, S, M, and UH are the count rates in the 0.3−0.5, 0.5−2, 2−4.5, and 4.5−10 keV band, respectively; (col. [18]) the pointing ID at which the source is detected; (col. [19]) the offset angle from the mean optical axis in the corresponding pointing; (col. [20]) the total pn-equivalent exposure (sum of pn, MOS1, and MOS2) at the source position, corrected for the vignetting in the 0.5−4.5 keV band; (col. [21]) the background rate in the 0.5−4.5 keV band at the source position; (col. [22]) the flag if the flux is determined by

TABLE 5
FLUX CONVERSION FACTORS

ASSUMED SPECTRUM PHOTON INDEX	FLUX CONVERSION FACTORS[a]					
	0.3−0.5 keV Band	0.5−2 keV Band	2−4.5 keV Band	4.5−10 keV[b] Band	0.5−4.5 keV Band	2−10 keV[b] Band
1.0..............................	0.164	0.171	0.574	1.718	0.305	1.057
1.1..............................	0.167	0.171	0.571	1.696	0.295	1.026
1.2..............................	0.171	0.170	0.568	1.675	0.285	0.996
1.3..............................	0.174	0.170	0.564	1.653	0.276	0.967
1.4..............................	0.177	0.169	0.561	1.632	0.267	0.939
1.5..............................	0.181	0.168	0.558	1.612	0.259	0.912
1.6..............................	0.184	0.168	0.555	1.593	0.250	0.886
1.7..............................	0.187	0.167	0.551	1.573	0.243	0.862
1.8..............................	0.190	0.167	0.548	1.554	0.236	0.838
1.9..............................	0.194	0.167	0.545	1.536	0.229	0.816
2.0..............................	0.197	0.166	0.541	1.517	0.223	0.794

[a] The conversion factor from the vignetting-corrected, pn-equivalent count rate into energy flux between the same band in units of $[10^{-14}$ erg cm^{-2} s$^{-1}]/[$counts ks$^{-1}]$. The fluxes are corrected for Galactic absorption of $N_{\rm H} = 2.5 \times 10^{20}$ cm^{-2}.
[b] The 7.9−8.3 keV band is excluded in the count rate but included in the flux.
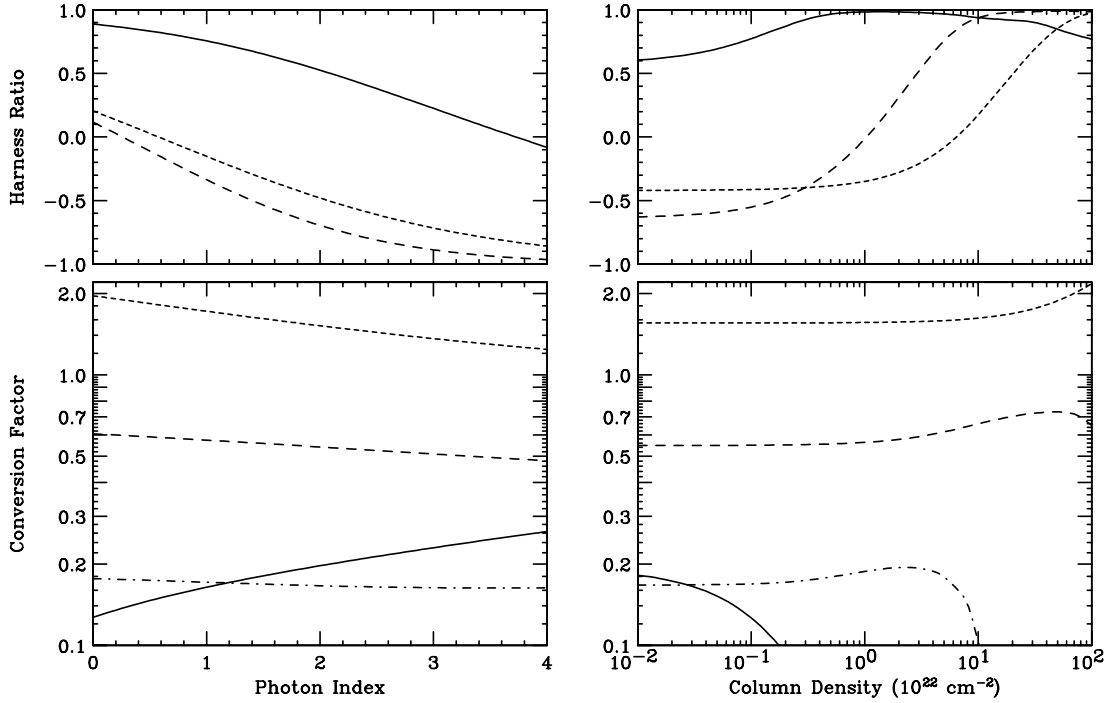
FIG. 2.—*Bottom*: Conversion factors from the vignetting-corrected count rate into flux in the same band, calculated for different spectra. The unit is [10^{-14} ergs cm^{-2} s^{-1}/(counts ks^{-1})]. The solid, dot-dashed, long-dashed, and short-dashed curves correspond to the 0.3–0.5, 0.5–2, 2–4.5, and 4.5–10 keV bands, respectively. *Top*: Hardness ratio expected from the assumed spectra. The solid, long-dashed, and short-dashed curves correspond to HR1, HR2, and HR3, respectively. (*a*) *Left*: the parameter is a photon index of a power law with no absorption. (*b*) *Right*: the parameter is an absorption column density for a power-law spectrum with a photon index of 1.8.

multiple-source fit to take into account possible source confusion with nearby sources (see § 3.2.3). The exposure and background rate (cols. [20] and [21]) are averaged over the source extraction region with a fixed encircled energy fraction (68%) of the PSF. From the results of optical identification (M. Akiyama et al. 2008, in preparation), we confirm that the positional errors given in this list are reasonable. In Table 3 we list the spatial extent and its likelihood of all the extended sources contained in Table 2.

We detect 1245 sources in total. The numbers of detected sources in a single or two bands in any combination from the six energy bands are summarized in Table 4. According to simulation study,[16] the number of fake sources due to statistical fluctuation is

[16] See http://xmmssc-www.star.le.ac.uk/newpages/1XMM/fig_5.3.html.

estimated to be about 1.5 per pointing in each energy band at our likelihood threshold ($ML \geq 7$), hence ≈ 50 in the sum sample. Their fraction in the total number of detected sources depends on the selection band; it becomes the smallest (0.6%) in the 0.5–4.5 keV but largest (5%) in the 4.5–10 keV band because of different sensitivities.

We calculate the conversion factors from a count rate into a flux in each energy band by using the energy response of the pn. Galactic absorption of $N_H = 2.5 \times 10^{20}$ cm^{-2} (Dickey & Lockman 1990) is taken into account. The values are summarized in Table 5 for a power-law spectrum with various photon indices (Γ). Figure 2a shows their dependence on the photon index assuming no absorption, whereas in Figure 2b we change the absorption column density at zero redshift for a fixed photon index of 1.8. In
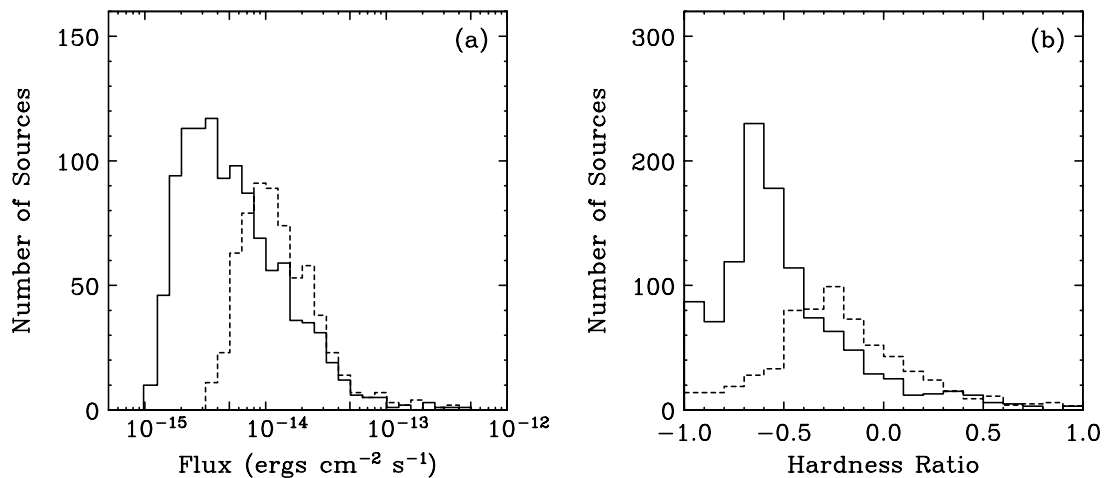

FIG. 3.—*Left*: Histogram of flux for the 0.5–4.5 keV (*solid line*) and 2–10 keV (*dashed line*) selected sample in the SXDS *XMM-Newton* catalog. *Right*: That of hardness ratio HR2 (*solid line*) and HR3 (*dashed line*) for the 0.5–4.5 and 2–10 keV selected sample, respectively.
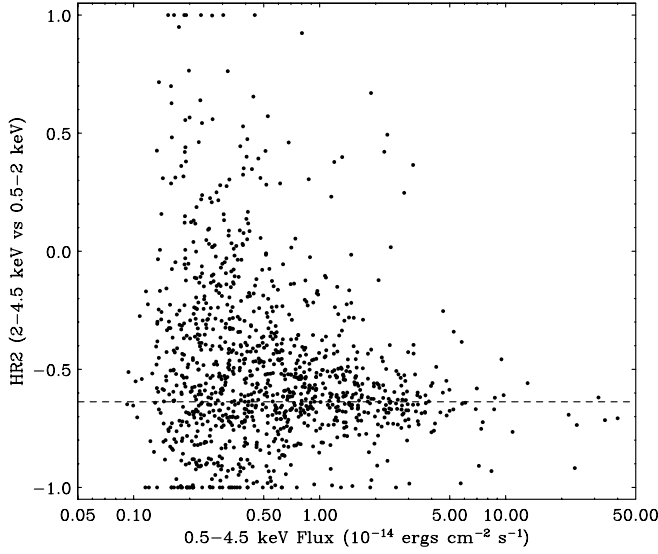
Fig. 4.—The 0.5–4.5 keV flux vs. HR 2 plot for the sources detected in the 0.5–4.5 keV band. HR 2 is defined as $(M - S)/(M + S)$, where M and S is the vignetting-corrected pn-equivalent count rate in the 2–4.5 and 0.5–2 keV bands, respectively. The dashed line corresponds to a power-law photon index of 1.8.

Fig. 5.—The 2–10 keV flux vs. HR 3 plot for the sources detected in the 2–10 keV band. HR 3 is defined as $(H - M)/(H + M)$, where H and M is the vignetting-corrected pn-equivalent count rate in the 4.5–10 and 2–4.5 keV bands, respectively. The dashed line corresponds to a power-law photon index of 1.8.

the same figures we also plot the hardness ratios HR 1, HR 2, and HR 3 as a function of spectral parameters. For the flux conversion, hereafter we assume $\Gamma = 1.5$ (with no absorption) for the 2–4.5, 4.5–10, 0.5–4.5, and 2–10 keV bands, and $\Gamma = 2.0$ for the 0.3–0.5 and 0.5–2 keV band, unless otherwise mentioned.

3.4. Spectral Properties of the Sources

In this subsection, we summarize spectral properties of the SXDS sources based on hardness ratio analysis using the above source list. Figure 3a shows the flux distribution of sources detected in the 0.5–4.5 and 2–10 keV bands. As described below, our sample covers X-ray sources that constitute a major fraction of the XRB below 10 keV. Figure 3b shows the histogram of hardness ratio HR 2 and HR 3 for those detected in the 0.5–4.5 and 2–10 keV bands, respectively. The flux versus hardness ratio plots are given in Figure 4 (0.5–4.5 keV flux vs. HR 2) and Figure 5 (2–10 keV flux vs. HR 3). For clarity we do not attach error bars to each point in these figures; the typical 1 σ errors in HR 2 and HR 3 are 0.22 and 0.15 at flux levels of $(2-4) \times 10^{-15}$ erg cm^{-2} s^{-1} (0.5–4.5 keV) and $(1-2) \times 10^{-14}$ ergs cm^{-2} s^{-1} (2–10 keV), respectively. To examine the mean spectral properties as a function of flux, we produce flux-weighted spectra in the four bands from flux-range–limited samples, by summing up the count rate of the individual sources in each energy band. Table 6 summarizes their HR 2 and HR 3 values with corresponding power-law photon indices. We find evidence that the spectra of the X-ray sources becomes harder at fainter fluxes with a confidence level of 99.99% (HR 2) and 96% (HR 3) for the 0.5–4.5 keV sample but with a lower confidence level of 84% (HR 2) and 90% (HR 3) for the 2–10 keV sample. Their mean slope is similar or even harder than that of the XRB, $\Gamma \simeq 1.4$ over the 0.5–10 keV band at these flux levels. This result is consistent with the fact that we already resolved a major parts of the XRB and that at brighter fluxes where 20%–30% of the XRB is produced, the mean spectra are much softer than the XRB spectrum (Ueda et al. 1999).

Figure 6 shows the color-color plot between HR 2 and HR 3 by using 208 sources detected in the 0.5–4.5 and/or 2–10 keV band whose statistical errors in both hardness ratios are smaller than 0.2. The solid curve tracks the color of a power-law spectrum with
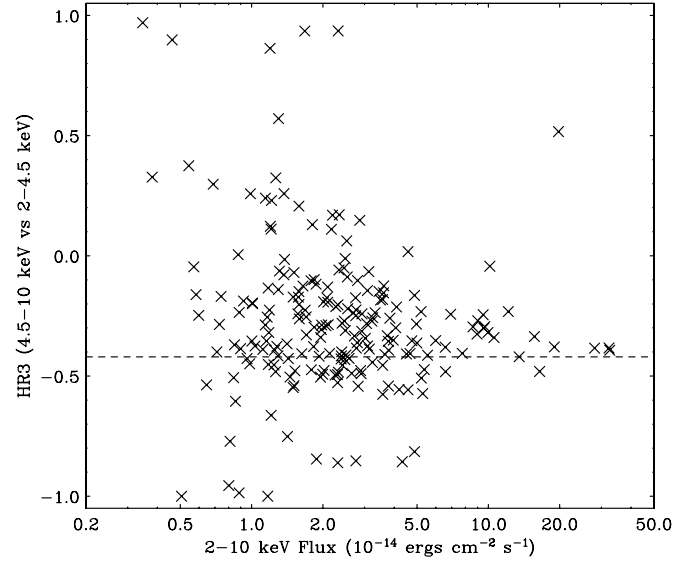
varying photon indices from 0 to 4, while the dashed curve does that with varying absorption column densities at $z = 1$ (a typical redshift of our sample; see Fig. 14) from log $N_H = 0$ to 24 for a fixed photon index of 1.8. As noticed, the spectra of some sources are not simply represented by an absorbed power-law model. In particular, there is a population of sources that are hard in the 2–10 keV band (e.g., HR 3 $\gtrsim 0$) but soft in the 0.5–4.5 keV band (HR 2 $\lesssim 0$), indicating the presence of additional soft components. Detailed spectral analysis using information of redshift will be presented in forthcoming papers.

4. log N–log S RELATION

4.1. Sensitivity Map

To make statistical analysis using the source list, such as determination of the log N–log S relation, it is crucial to have reliable sensitivity maps for each pointing and energy band—i.e., we need to know a flux (count rate) limit as a function of position at a given detection criterion (i.e., ML ≥ 7). Since we utilize the maximum likelihood algorithm, however, it is not trivial to calculate sensitivities by employing an analytic formula, unlike in the case of cell detection. Ideally, only a detailed simulation can give the correct estimate of a sensitivity at every position, since it depends on the background, exposure map, and PSF in a complex way. To save computing time, we here take an empirical approach by utilizing both simulation and analytical calculation, as described below.

First, we directly estimate the flux limit by *simulation* at two-dimensional grid points with $40''$ spacing over the FOV. For a given position, we produce a simulated image where a point source is superimposed on an input background map, using the `emldetect` program. Since we are looking simply for a relation between the `emldetect` ML value and the flux of the sources, we do not taken into account Poisson counting noise in our simulation. We then perform a likelihood fit with `emldetect` to the simulated image and derive the ML value for the input source. Repeating the simulation assuming several different fluxes for the point source, we obtain an empirical relation between the input flux and output ML value. This relation enables us to calculate the sensitivity for a given threshold of ML at that position.

TABLE 6
Average Hardness Ratio for Flux-limited Samples

Sample			Average Spectra[a]			
			0.5–4.5 keV Band		2–10 keV Band	
Detection Band	Flux Range $(10^{-14}$ erg s^{-1} cm$^{-2})$	Number of Sources	$\langle HR2 \rangle$	$\langle \Gamma_{0.5-4.5} \rangle$	$\langle HR3 \rangle$	$\langle \Gamma_{2-10} \rangle$
0.5–4.5 keV	0.5–2.0	406	-0.55 ± 0.01	1.55 ± 0.02	-0.27 ± 0.02	1.34 ± 0.05
0.5–4.5 keV	2.0–8.0	107	-0.61 ± 0.01	1.71 ± 0.02	-0.33 ± 0.02	1.52 ± 0.05
2–10 keV	1.0–4.0	334	-0.53 ± 0.01	1.50 ± 0.02	-0.23 ± 0.02	1.23 ± 0.04
2–10 keV	4.0–16	38	-0.55 ± 0.01	1.55 ± 0.02	-0.29 ± 0.03	1.40 ± 0.08

[a] The averaged hardness ratio is derived the summed spectrum of the flux-limited sample. The corresponding power-law photon index in the same band is also shown, which is corrected for Galactic absorption of $N_H = 2.5 \times 10^{20}$ cm^{-2}. The error is 1 σ.

Next, we produce full resolution (4″ pixel) sensitivity maps by *interpolating* between the grid points in the following manner. The flux limit could change quite sensitively with the position, being affected by data gaps between CCD gaps or hot pixel regions. A simple interpolation of the flux limit based on the rough position sampling in the above simulation may not be sufficiently accurate. To estimate the precise position dependence, we utilize analytical sensitivity maps calculated by the `esensmap` program, which is based on the cell detection algorithm. Generally, the detection likelihood obtained by `emldetect` (ML) differs from that defined in the cell detection (ML_{cell}) for the same flux. The ratio between ML and ML_{cell} should be a function of position, primarily depending on the size and shape of the PSF. Hence, we calculate the ML_{cell} value corresponding to the flux limit at each grid point and interpolate them between the grid points as a linear function of position. We finally convert ML_{cell} into a "flux limit" at each position, by referring to a set of sensitivity maps calculated by `esensmap` with different thresholds of ML_{cell}, thus producing
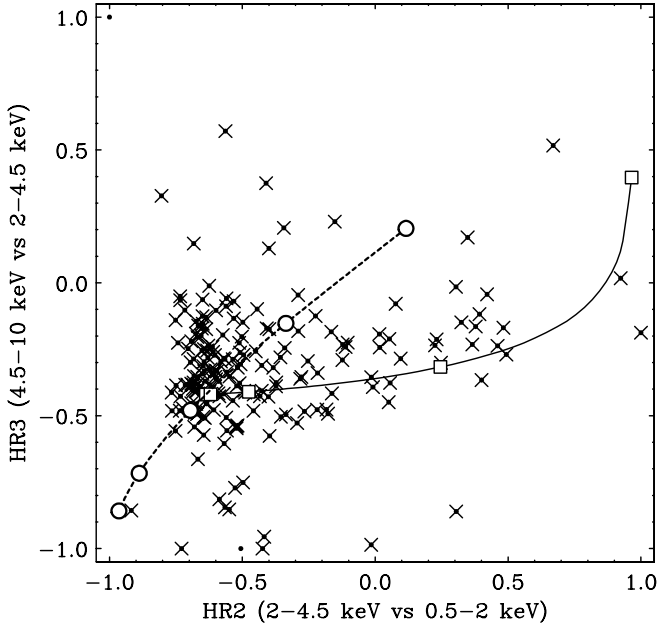
the final sensitivity maps. To evaluate systematic errors in the sensitivity map, we compare the results when the positions of the grid points are shifted by 20″ in each direction. We find that the difference in the flux limit is mostly within a few percent and <10% at maximum. We regard this (10%) as the maximum relative systematic error in the sensitivity map, which will be considered in the analysis of the spatial distribution of sources (§ 5.2).

4.2. Results and Comparison with Other Work

Superposing the sensitivity maps of the seven pointings in the common sky coordinates, we examine, position by position, in which pointing data the best sensitivity is achieved in the 0.5–4.5 keV band in overlapping regions. As mentioned above, we only refer to the results of a single pointing, at given sky coordinates, to obtain the combined source list and sensitivity maps to eliminate duplication. The resultant sensitivity map in the 0.5–4.5 keV band is shown in Figure 7. Figure 8 shows the area curves $\Omega(S)$ for ML ≥ 7 (i.e., survey area where the detection completeness is guaranteed above the given flux) obtained from the combined SXDS field in the four energy bands, 0.5–2, 0.5–4.5, 2–10, and 4.5–10 keV.
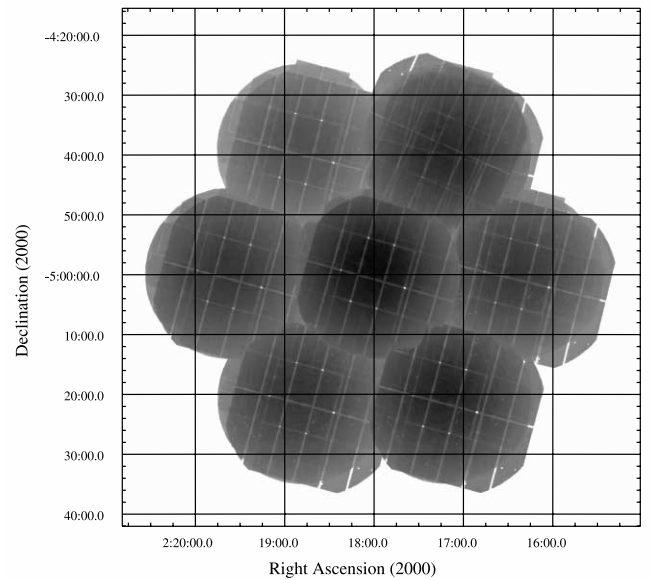

Fig. 6.—Color-color plot between HR2 and HR3. Only sources with a 1 σ uncertainty less than 0.2 in both HR2 and HR3 are included in the plot. The solid curve tracks the colors of an absorbed power-law spectrum for a fixed photon index of 1.8 with varying column densities (*from left to right*, log N_H cm^{-2} = 0, 21, 22, 23, 24 at $z = 1$), while the dashed curve does so for varying photon indices (*from left to right*, $\gamma = 4, 3, 2, 1, 0$) with no absorption. [*See the electronic edition of the Supplement for a color version of this figure.*]

Fig. 7.—Sensitivity map in the 0.5–4.5 keV band. The minimum flux threshold for the detection likelihood ≥7 is given as a function of position in the sense that a darker color corresponds to a lower flux. SDS-2 is located to the east of the central field, SDS-1, and SDS-3 through 7 go in a clockwise direction after SDS-2.
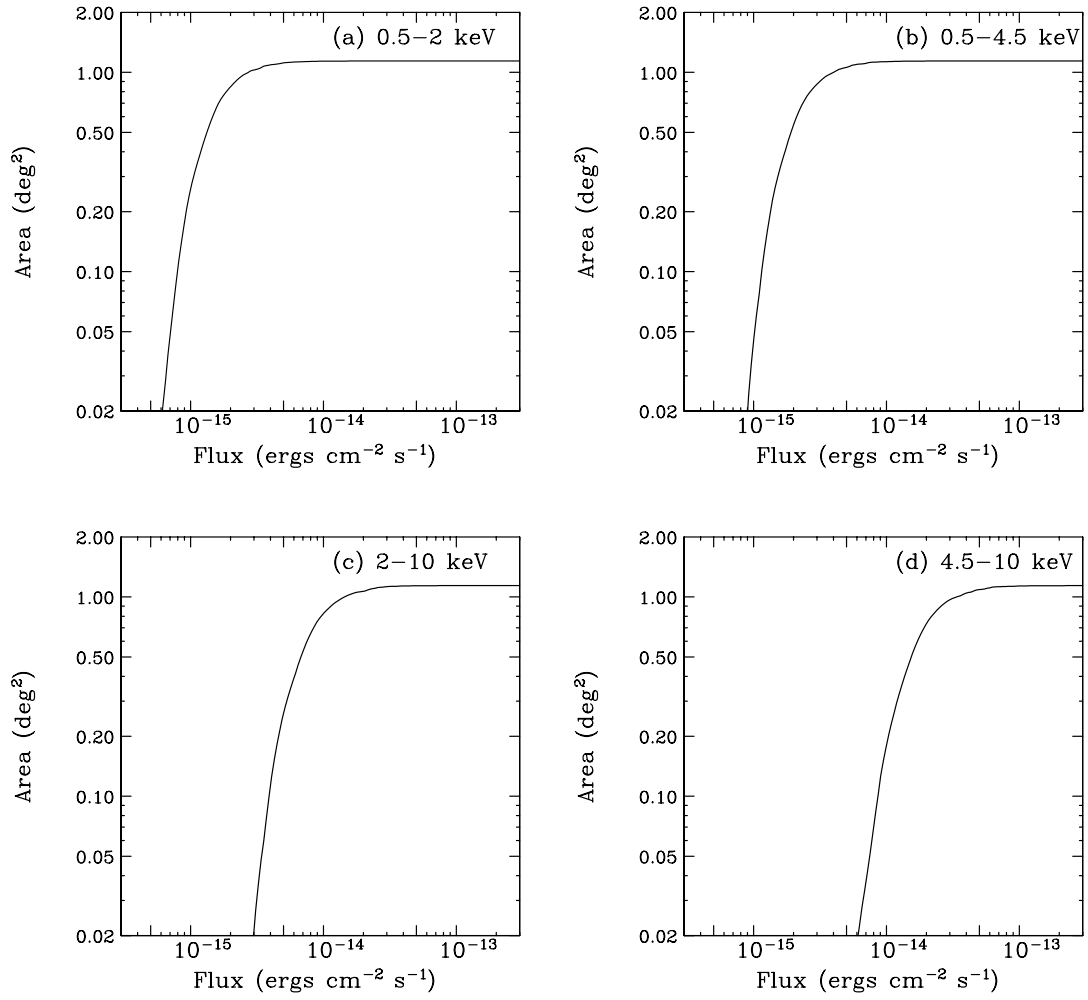
FIG. 8.—Survey area given as a function of flux in the whole SXDS field in the (*a*) 0.5–2, (*b*) 0.5–4.5, (*c*) 2–10, and (*d*) 4.5–10 keV bands.
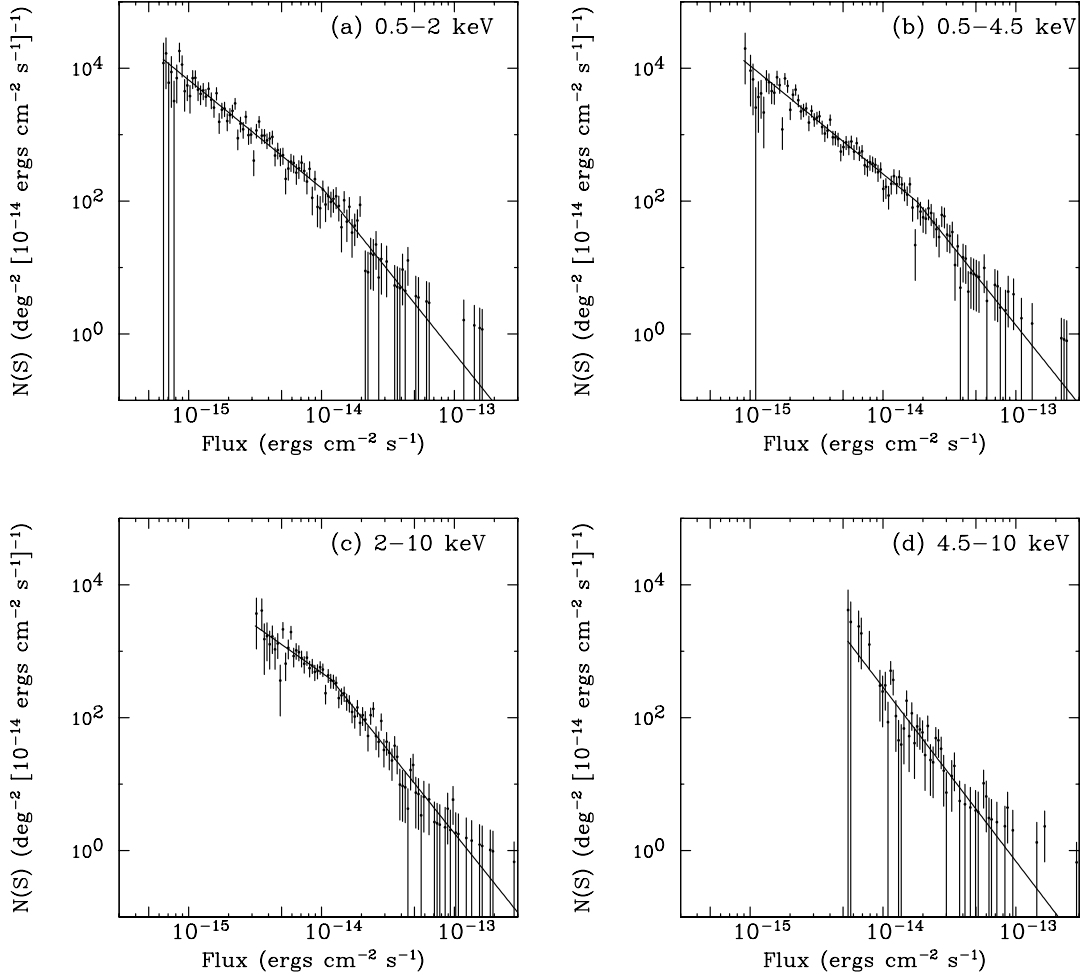
FIG. 9.— Differential log N–log S relations in the (*a*) 0.5–2, (*b*) 0.5–4.5, (*c*) 2–10, and (*d*) 4.5–10 keV bands. The attached errors correspond to 1 σ Poisson error one in the number of sources. The solid lines are the best-fit broken power-law model (see eq. [1] and Table 7). [*See the electronic edition of the Supplement for a color version of this figure.*]

Dividing the observed flux distribution by $\Omega(S)$, we first obtain the log N–log S relations in the differential form, $N(S)$. Here we discard sources whose flux falls below the sensitivity limit at the give position because we consider that such detection may not be reliable. Figure 9 shows $N(S)$ in the four bands in units of number per square degree per 10^{-14} ergs cm^{-2} s^{-1}, where the errors represent the 1 σ Poisson error in the number of sources in each flux bin. Following previous work, we fit them with a broken power-law form, expressed as

$$N(S) = \begin{cases} \dfrac{K}{S_b}\left(\dfrac{S}{S_b}\right)^{-\Gamma_d}, & (S \leq S_b), \\[2ex] \dfrac{K}{S_b}\left(\dfrac{S}{S_b}\right)^{-\Gamma_u}, & (S > S_b). \end{cases} \quad (1)$$

The model has a break flux S_b, above and below which the slope is Γ_u and Γ_d, respectively. To estimate the parameters, we utilize a maximum likelihood method, so that the model best reproduces the observed flux distribution expected from the area curve. We fix Γ_u at 2.5 in the 0.5–2, 0.5–4.5, and 2–10 keV bands, while in the 4.5–10 keV band, we adopt a single power law by setting $\Gamma_d = \Gamma_u$ and $S_b = 1 \times 10^{-14}$ ergs cm^{-2} s^{-1} because the break is not evident in our flux range. The best-fit models are shown in solid lines in Figure 9. Table 7 summarizes the best-fit parameters, which are

found to be consistent with previous results within uncertainties (e.g., Carrera et al. 2007; Brunner et al. 2008).

The differential log N–log S relations are then integrated toward lower fluxes to produce the log N–log S relations in the integral form, $N(>S)$, where the number density of sources with fluxes above S is plotted (Fig. 10). The achieved sensitivities, defined as the fluxes at which the sky area falls below 1% of the maximum area (1.14 deg^2), are 6×10^{-16}, 8×10^{-16}, 3×10^{-15}, and 5×10^{-15} ergs cm^{-2} s^{-1} in the 0.5–2, 0.5–4.5, 2–10, and 4.5–10 keV bands: above these fluxes $(88 \pm 5)\%$, $(75 \pm 3)\%$, $(74 \pm 4)\%$, and $(52 \pm 3)\%$ of the XRB are resolved, when we adopt the XRB intensity of $(7.5 \pm 0.4) \times 10^{-12}$, $(15.3 \pm 0.6) \times 10^{-12}$, $(20.2 \pm 1.1) \times 10^{-12}$, and $(12.3 \pm 0.7) \times 10^{-12}$ erg cm^{-2} s^{-1} deg^{-2}, respectively, taken from Table 6 of Carrera et al. (2007)

TABLE 7
BEST-FIT PARAMETERS FOR log N–log S RELATIONS

Band	Γ_u	Γ_d	S_b (10^{-14} cgs)	K (deg^{-2})
0.5–2 keV	2.5 (fixed)	$1.63^{+0.07}_{-0.12}$	$1.03^{+0.25}_{-0.29}$	154^{+63}_{-32}
0.5–4.5 keV	2.5 (fixed)	$1.63^{+0.06}_{-0.09}$	$1.81^{+0.44}_{-0.40}$	177^{+52}_{-36}
2–10 keV	2.5 (fixed)	$1.41^{+0.17}_{-0.20}$	$1.19^{+0.13}_{-0.15}$	444^{+66}_{-58}
4.5–10 keV	$2.62^{+0.13}_{-0.12}$	...	1.0 (fixed)	288^{+40}_{-36}

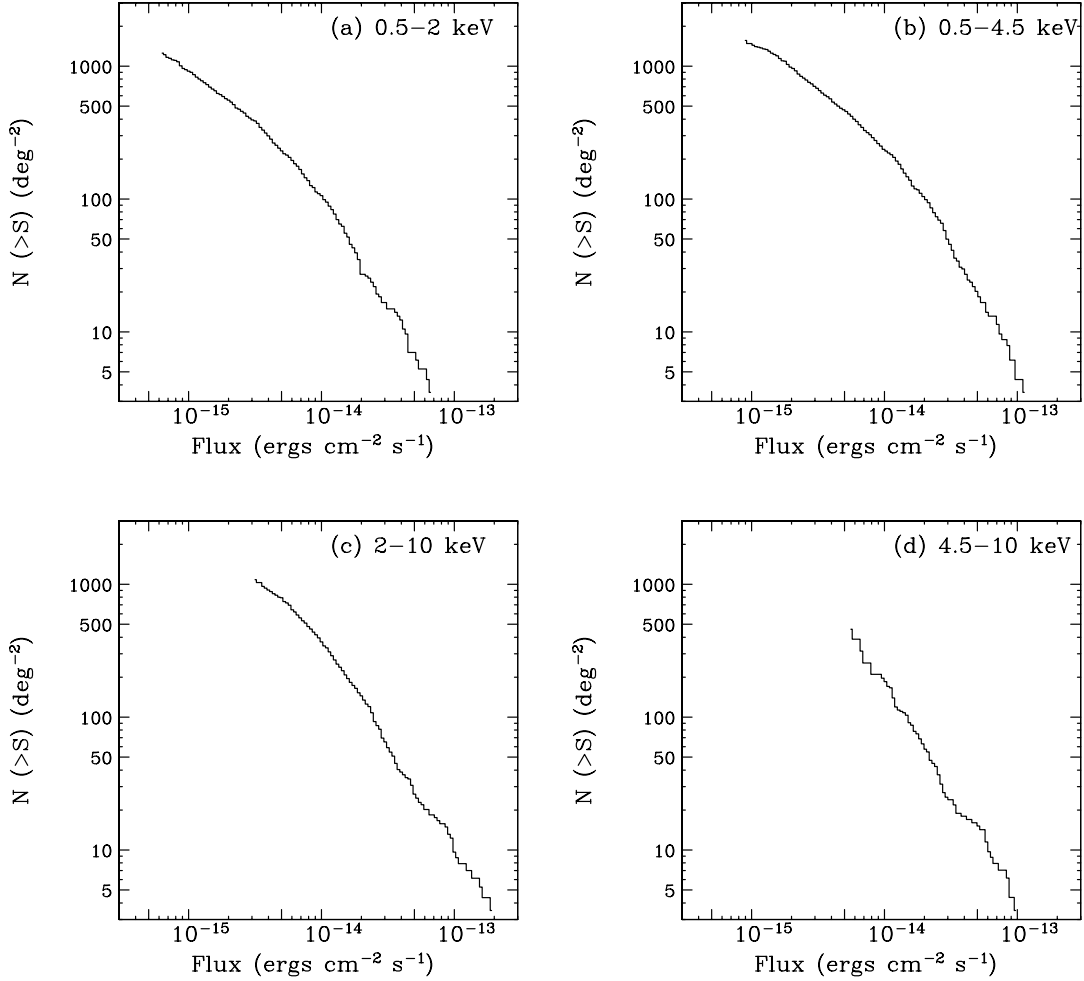NOTE.— The error is 1 σ for a single parameter.

Fig. 10.—The log N–log S relation obtained from the whole SXDS field in the (*a*) 0.5–2, (*b*) 0.5–4.5, (*c*) 2–10, and (*d*) 4.5–10 keV bands.

with an appropriate flux conversion for the 4.5–10 keV band. For the estimate of the contribution of bright sources that is not well constrained from the SXDS data, we have used the formula by Carrera et al. (2007), who complied the results from *Chandra* deep surveys, *XMM-Newton* serendipitous surveys, and the *ASCA* medium sensitivity survey.

Figure 11 shows the same log N–log S relations scaled by $(S/10^{-14})^{1.5}$ to stress the deviation from a Euclidean slope. The dashed curves represent the best-fit formula by Carrera et al. (2007); they are plotted in the figure covering only the region where the fit is performed. Our results are in good agreement with the previous work within $\approx$10%, indicating systematic errors, if any, are confined within this level. The open circles are the results of the COSMOS survey (Cappelluti et al. 2007). Here we convert the result by Carrera et al. (2007) in the 4.5–7.5 keV band and that by Cappelluti et al. (2007) in the 5–10 keV band to the 4.5–10 keV band assuming a photon index of 1.5 (the flux conversion factor is 1.686 and 1.124, respectively). As seen from the figure, the COSMOS source counts in the 2–10 keV band are 20%–30% smaller than ours and the Carrera et al. (2007) results. This is most probably because, while our results are truly based on the 2–10 keV survey, Cappelluti et al. (2007) make this plot from the 2–4.5 keV survey by converting the flux into the 2–10 keV band assuming a photon index of 1.7. This could easily miss a population of sources with hard spectra or underestimate their fluxes. In the 0.5–2 keV band, our source counts at $S < 3 \times 10^{-14}$ erg cm^{-2} s^{-1}

are systematically larger than both Carrera et al. (2007) and Cappelluti et al. (2007) but are consistent with the latest results from the *XMM-Newton* Lockman Hole survey (Brunner et al. 2008).

5. CLUSTERING OF SOURCES

5.1. *Spatial Distribution*

Investigating the evolution of the large scale structure of the universe is one of the main scientific objectives of the SXDS. From X-ray surveys, we can study the clustering properties of AGNs including both unobscured and obscured populations over a wide redshift range as a tracer of the large-scale structure. This also helps us to understand the AGN phenomena and their environment by measuring the mass of underlying dark matter halo where the AGN activity took place.

Many studies have shown the presence of the significant large scale structure in the spatial (both two-dimensional and three-dimensional) distribution of X-ray sources (e.g., Vikhlinin & Forman 1995; Carrera et al. 1998, 2007; Akylas et al. 2000; Yang et al. 2003; Gilli et al. 2003, 2005; Basilakos et al. 2004, 2005; Mullis et al. 2004; Yang et al. 2006; Puccetti et al. 2006; Gandhi et al. 2006; Miyaji et al. 2007). This leads pencil beam surveys to be inevitably subject to cosmic variance. The SXDS, thanks to its wide and continuous area coverage, provides us with an ideal opportunity to investigate this issue. Figure 12 shows the location
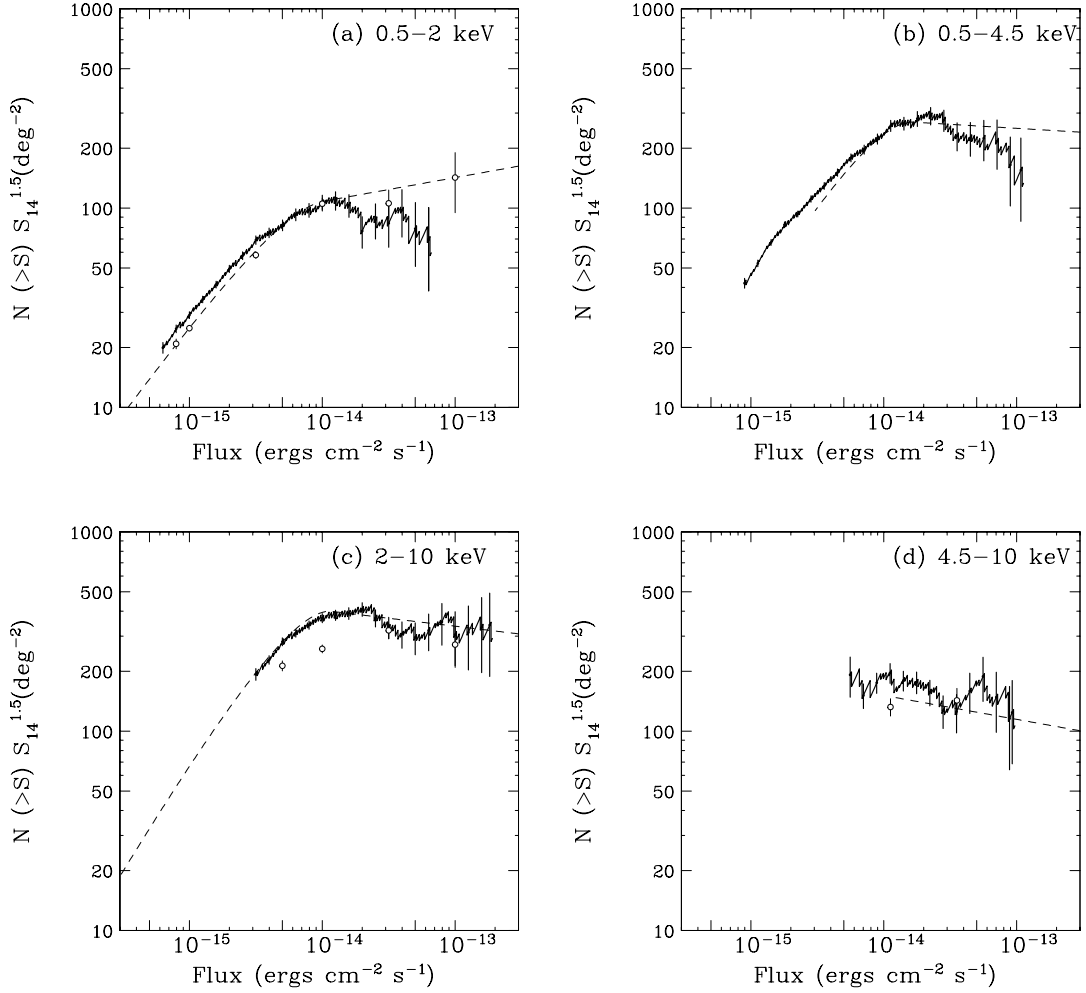
FIG. 11.—The log N–log S relation obtained from the whole SXDS field in the (*a*) 0.5–2, (*b*) 0.5–4.5, (*c*) 2–10, and (*d*) 4.5–10 keV bands, scaled by $(S/10^{-14})^{1.5}$. The error bars in our data correspond to 1 σ statistical errors. The dashed curves correspond to the best-fit model by Carrera et al. (2007) obtained by using *Chandra*, *XMM-Newton*, and *ASCA* results. The open circles are the results obtained from the COSMOS survey (Cappelluti et al. 2007). In (*d*), both results are converted into the 4.5–10 keV band assuming a photon index of 1.5. [*See the electronic edition of the Supplement for a color version of this figure.*]
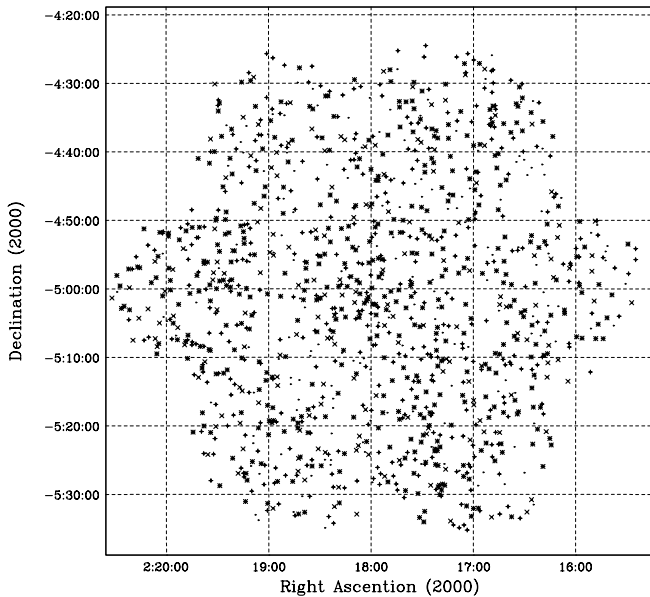
FIG. 12.—Spatial distribution of detected X-ray sources in the whole SXDS field. Crosses, dots, and diagonal crosses correspond to those detected in the 0.5–2, 0.5–4.5, and 2–10 keV band, respectively.

of sources detected in the 0.5–2, 0.5–4.5, or 2–10 keV band (with ML $\geq$ 7) in our source catalog. Figure 13 shows the log N–log S relations separately derived from the seven pointings. As done in the analysis of § 3.3, here we excluded any data with shorter exposures in overlapping regions of multiple pointings, and hence the results are statistically independent one another. It can be seen that the source counts show significant variation among the pointings, depending on the flux limit. In particular, those of SDS7 in the 0.5–2 and 0.5–4.5 keV band are by more than 30% smaller than the other fields in the medium to high flux range. These results indicate that the cosmic variance indeed exists over an area scale of one *XMM-Newton* FOV, ~0.2 deg^2, which is much larger than the FOV of *Chandra* observatory.

5.2. Autocorrelation Function

The most straightforward approach to quantify the clustering properties of sources is to calculate the angular two-point correlation function (or autocorrelation function [ACF]). The ACF, $w(\theta)$, is defined as
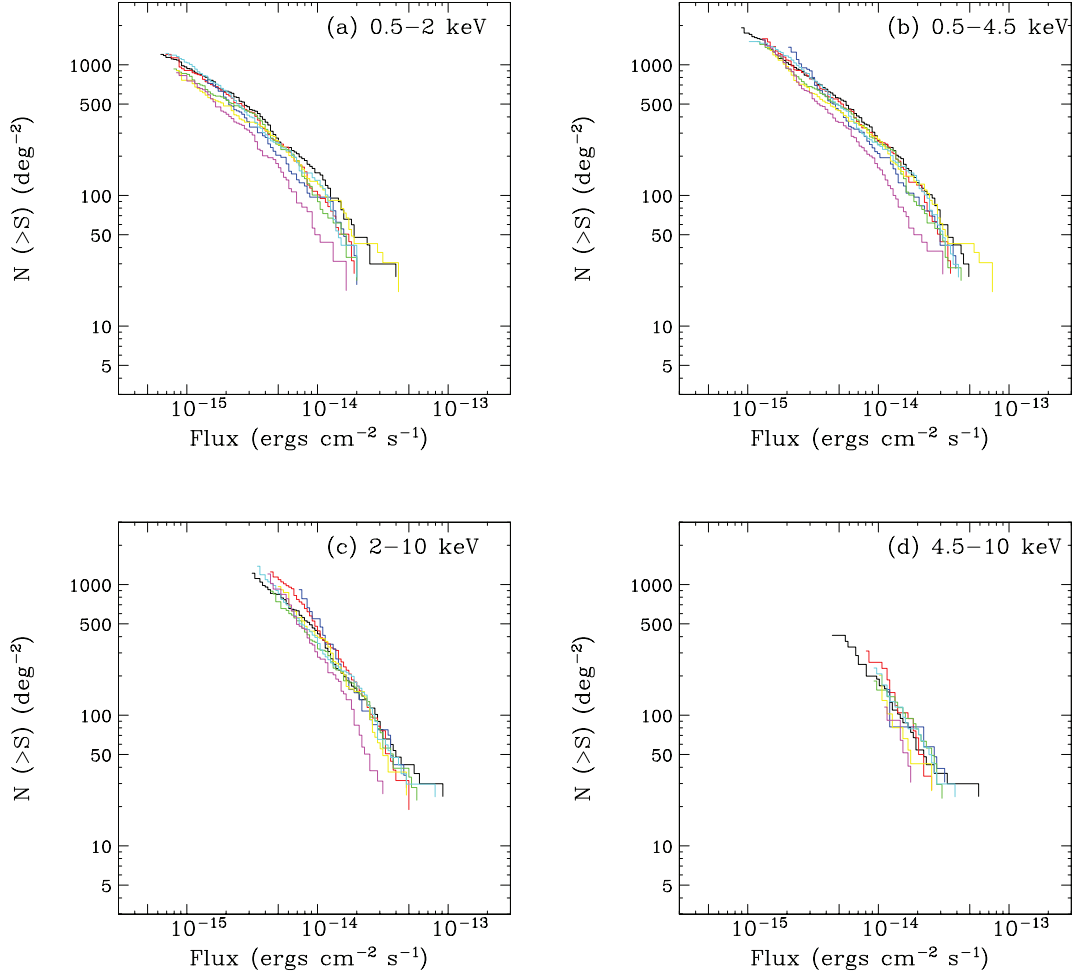
$$dP = n^2[1 + w(\theta)]d\Omega_1 d\Omega_2,$$

Fig. 13.— The log *N*–log *S* relation for each field in the (*a*) 0.5–2, (*b*) 0.5–4.5, (*c*) 2–10, and (*d*) 4.5–10 keV band. *Black*: SDS-1; *red*: SDS-2; *blue*: SDS-3; *green*: SDS-4; *yellow*: SDS-5; *cyan*: SDS-6; *magenta*: SDS-7. In the overlapping regions between different pointings data of lower exposure are excluded in the analysis, i.e., the plots are statistically independent of one another.

where *dP* gives the probability of finding a pair of two objects located at the differential solid angle of Ω_1 and Ω_2 with a separation angle of θ, and *n* is the mean number density.

To estimate the ACF, we essentially follow the same procedure as done in Miyaji et al. (2007). We adopt the Landy & Szalay (1993) estimator,

$$w_{\mathrm{obs}}(\theta) = \frac{DD - 2DR + RR}{RR},$$

where *DD*, *DR*, and *RR* are the normalized number of data-data pairs, data-random pairs, and random-random pairs, respectively. In calculating the ACF, it is critical to ensure that the sensitivity map is correctly modeled at every position. Hence, considering possible position-dependent systematic errors in the sensitivity maps created in § 4.1, we introduce a "safety factor," $f = 1.1$, to multiply the nominal sensitivity limits and select only sources whose observed flux is higher than the (corrected) sensitivity limit at the detected position. The choice of $f = 1.1$ is quite conservative, and indeed we obtain essentially the same results even when $f = 1.0$ is adopted. We make a random sample whose number is 10 times that of the actual data. The flux distribution of the random sample is taken to be the same as in the actual source list, and their positions are randomly distributed by satisfying that the

flux must be higher than the sensitivity limit at the allocated position.

Figure 14 shows our results of the ACF obtained in the 0.5–2 and 2–10 keV bands. The flux range and number of sources used in the analysis are summarized in the second and third columns of Table 8, respectively. The attached error is estimated by simulation: we produce 100 sets of random samples with the same source number as in the data, obtain a standard deviation of the ACF signal obtained by the same procedure as applied for the actual data, and then multiplied it by $[1 + w(\theta)]^{1/2}$. We fit the ACF with a power-law form

$$w(\theta) = (\theta/\theta_c)^{1-\gamma}$$

in the range of $\theta = 0.5$–10 ′, considering the size of the PSF of *XMM-Newton*. We fix $\gamma = 1.8$ (Peebles 1980), which is difficult to constrain by our data, and derive the correlation length θ_c as a free parameter. To take into account the coupling of the ACF between different bins, we utilize the "covariance matrix," which is also obtained from the simulation of the random sample described above; we refer the readers to § 3.4 of Miyaji et al. (2007) for details. In the fit, we also consider an offset produced by the integral constraint, $\iint w(\theta) d\Omega_1 d\Omega_2 = 0$, assuming that the
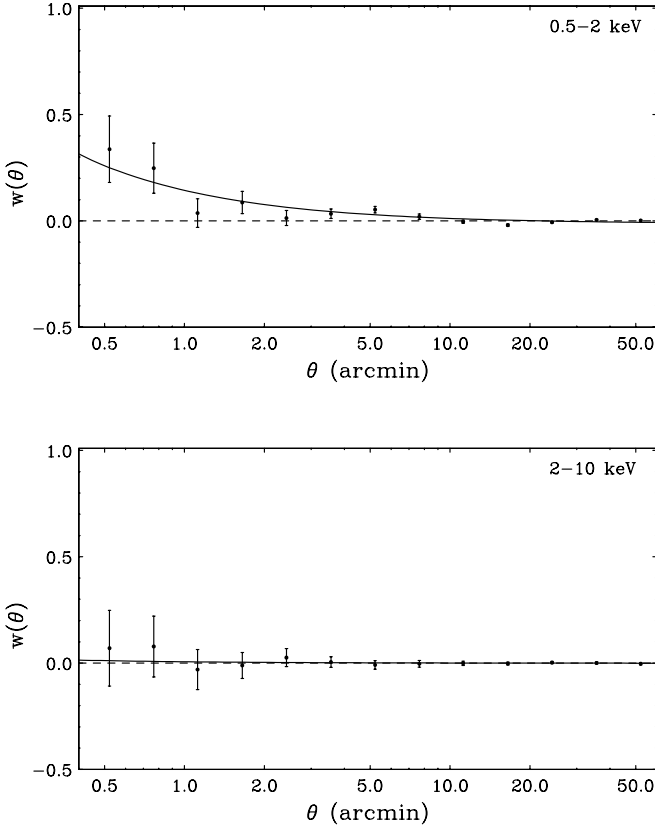
Fig. 14.—Autocorrelation function of the SXDS sources in the 0.5–2 and 2–10 keV bands. The errors are 1 σ. The solid curve represents the best-fit model (power law plus constant to account for the integration constraint).

Fig. 15.—Normalized redshift distribution of AGN in our samples selected in the 0.5–2 keV (*solid curve*) and 2–10 keV (*dashed curve*) bands, estimated from the model by Ueda et al. (2003).

power-law form of the ACF holds over the whole area. The obtained values of θ_c are listed in the sixth column of Table 8.

We detect an ACF signal from the 0.5–2 keV selected sample with $\theta_c = 5.9^{+1.0}_{-0.9}$ arcsec. The signal is not significantly found from the 2–10 keV sample, however, with a 90% confidence upper limit of $\theta_c < 1.5''$. By Limber's equation (Peebles 1980), the ACF can be transformed to the three-dimensional correlation function

$$\xi(r, z) = (r/r_{c,0})^{-\gamma}(1+z)^{-3-\epsilon+\gamma},$$

once the redshift distribution of the sample is known. Here we assume the comoving clustering model where the correlation length $r_{c,0}$ is constant in the comoving coordinates, hence $\epsilon = \gamma - 3$. Figure 15 shows the AGN redshift distribution for the 0.5–2 and 2–10 keV samples estimated from the model by Ueda
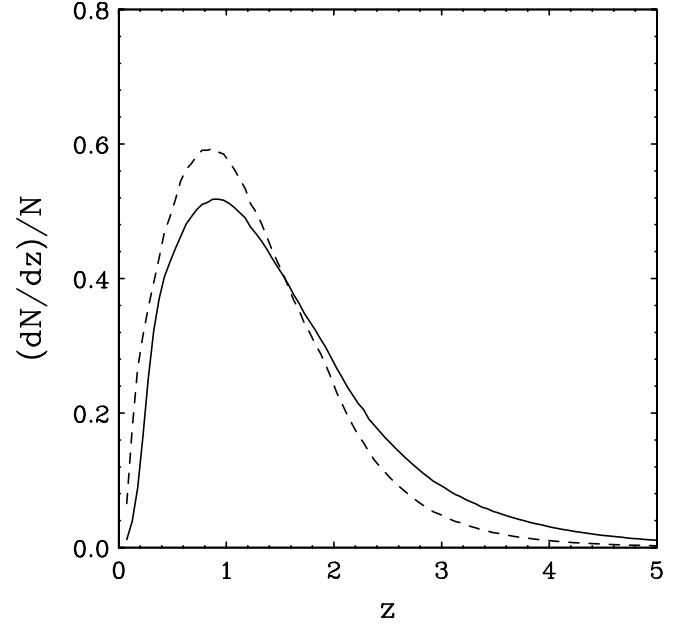
et al. (2003). From the θ_c values and redshift distribution, we finally obtain $r_{c,0} = 14.9 \pm 1.1\ h^{-1}$ Mpc and $r_{c,0} < 7.6\ h^{-1}$ Mpc with a medium redshift of 1.3 and 1.1 for the 0.5–2 and 2–10 keV selected sample, respectively. The bias parameter, the ratio of the rms fluctuation amplitude σ_8 (Peebles 1980) between AGNs and underlying mass, is found to be about 5.8 ± 0.5 for the 0.5–2 keV selected AGNs at a median redshift of 1.3.

The correlation length in the 0.5–2 keV is consistent with the previous results from soft X-ray surveys at similar redshift range reported by, e.g., Basilakos et al. (2005), Puccetti et al. (2006), and Carrera et al. (2007), although it is larger than those obtained from the optically selected QSOs (Croom et al. 2005). By contrast to several previous works that reported strong correlation of hard-band (>2 keV) selected samples (Yang et al. 2003; Basilakos et al. 2004), we find no evidence for significant clustering signals in the hard band. The detection of ACF in the 0.5–2 keV band but not in the 2–10 keV band is similar to what was found by Gandhi et al. (2006) and Carrera et al. (2007). It is curious that the first result from the *XMM-Newton* COSMOS survey reports a relatively large correlation length for the 4.5–10 keV band sample but smaller for the 2–4.5 keV band sample (Miyaji et al. 2007). Our 2–10 keV result is consistent with the COSMOS 2–4.5 keV result. We do

TABLE 8
CLUSTERING PROPERTIES OF THE X-RAY SOURCES

SAMPLE			CLUSTERING PROPERTIES				
Detection Band	Flux Range $(10^{-14}$ erg s^{-1} cm$^{-2})$	Number of Sources	$\theta_{min} - \theta_{max}$ (arcmin)	γ (Fixed)	θ_c[a,d] (arcsec)	z_{eff}[b]	r_c[c,d] $(h^{-1}$ Mpc)
0.5–2 keV	0.06–22	765	0.5–10	1.8	$5.9^{+1.0}_{-0.9}$	1.3	14.9 ± 1.1
2–10 keV....................................	0.32–33	573	0.5–10	1.8	0.1 (<1.5)	1.1	2.3 (<7.6)

[a] The two-dimensional correlation length, assuming a power-law form of $(\theta/\theta_c)^{1-\gamma}$ for the angular correlation function. The fit is performed between θ_{min} and θ_{max} with the integral constraint (see text).
[b] The median redshift contributing to the angular correlation.
[c] The correlation length assuming the comoving model ($\epsilon = \gamma - 3$), converted from θ_c via the Limber transformation (see text).
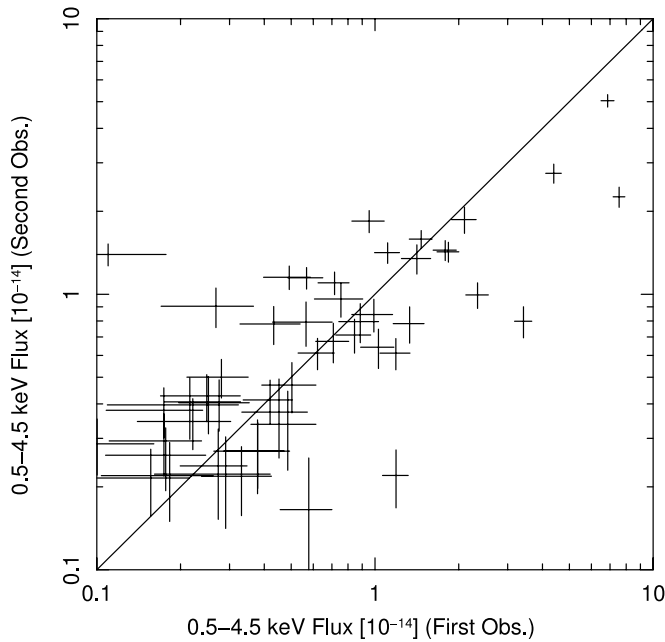[d] The error is 1 σ, while the upper limit is 90% confidence limit.

Fig. 16.—Comparison of the 0.5–4.5 keV flux measured in the two different epochs for sources detected in the SDS-4 field.

not find significant ACF signals from the 4.5–10 keV sample, although the result is more subject to the statistical fluctuation due to the small number of sources detectable in this energy band.

6. LONG-TERM X-RAY VARIABILITY OF SOURCES

We investigate the long-term variability of X-ray sources detected in the SDS-4 field, for which two observations were performed with a time separation of about 2.5 yr. The exposures of both observations are similar and are sufficiently long (>20 ks). Using the X-ray catalog produced from the combined images of the two observations, we examine the fluxes of the cataloged sources separately in each epoch by fixing their positions. To ensure high signal-to-noise ratio, we only use sources whose summed ML value from the 0.5–2 keV and 2–4.5 keV bands exceeds 15 in the combined catalog and vignetting-corrected exposure is longer than 15 ks in both observations. Figure 16 shows the comparison of the 0.5–4.5 keV flux between the first and second epochs for this sample. As noticed from the figure, many sources at interme-

diate fluxes that have sufficiently small error bars show a significant variability, demonstrating the impact of time variability in studying AGN properties. The results are consistent with previous studies (Paolillo et al. 2004; Mateos et al. 2007) reporting that the fraction of variable sources on timescales of months to years is 80%–90% or higher in *Chandra* and *XMM-Newton* deep fields.

7. SUMMARY

We have presented the first X-ray source catalog and their basic X-ray properties in the SXDS field, based on the seven *XMM-Newton* pointings performed between 2000 and 2003 that cover a continuous area of 1.14 deg^2 in the 0.2–10 keV band. The catalog consists of 1245 sources in total, consisting of those detected either in the 0.3–0.5, 0.5–2, 2–4.5, 4.5–10, 0.5–4.5, and 2–10 keV with detection likelihood larger than 7. From empirical sensitivity maps derived by simplified simulation, we obtain log N–log S relations in various energy bands bands, which bridge the flux range between *Chandra* deep surveys and brighter surveys. Clustering properties of X-ray sources are also studied by means of autocorrelation function. We detect significant signals that can be fitted by $(\theta/\theta_c)^{-0.8}$ with $\theta_c = 5.9^{+1.0}_{-0.9}$ arcsec for the 0.5–2 keV selected sample at an estimated median redshift of $z_{\rm eff} \approx 1.3$, and an 90% upper limit of $\theta_c < 1.5''$ for the 2–10 keV selected sample at $z_{\rm eff} \approx 1.1$. Two pointing data separated by 2.5 yr indicate the importance of flux variability on a timescale of years. Our results establish the average properties of X-ray sources at fluxes where a majority of the XRB is produced, being least affected by cosmic variance. The data presented here constitute a major component of the SXDS project and shall be used for a number of research programs in combination with other wavelength data.

REFERENCES

Akylas, A., Georgantopoulos, I., & Plionis, M. 2000, MNRAS, 318, 1036
Alexander, D. M., Brandt, W. N., Hornschemeier, A. E., Garmire, G. P., Schneider, D. P., Bauer, F. E., & Griffiths, R. E. 2001, AJ, 122, 2156
Alexander, D. M., et al. 2003, AJ, 126, 539
Barger, A. J., Cowie, L. L., Mushotzky, R. F., Yang, Y., Wang, W.-H., Steffen, A. T., & Capak, P. 2005, AJ, 129, 578
Basilakos, S., Georgakakis, A., Plionis, M., & Georgantopoulos, I. 2004, ApJ, 607, L79
Basilakos, S., Plionis, M., Georgakakis, A., & Georgantopoulos, I. 2005, MNRAS, 356, 183
Brandt, N., & Hasinger, G. 2005, ARA&A, 43, 827
Brunner, H., Cappelluti, N., Hasinger, G., Barcons, X., Fabian, A. C., Mainieri, V., & Szokoly, G. 2008, A&A, 479, 283
Cash, W. 1979, ApJ, 228, 939
Cappelluti, N., et al. 2007, ApJS, 172, 341
Carrera, F. J., et al. 1998, A&A, 299, 229
———. 2007, A&A, 469, 27
Cowie, L. L., Songaila, A., Hu, E. M., & Cohen, J. G. 1996, AJ, 112, 839
Croom, S. M., et al. 2005, MNRAS, 356, 415
Dickey, J. M., & Lockman, F. J. 1990, ARA&A, 28, 215
Ferrarese, L., & Merritt, D. 2000, ApJ, 539, L9

Franceschini, A., Hasinger, G., Miyaji, T., & Malquori, D. 1999, MNRAS, 310, L5
Furusawa, H., et al. 2008, ApJS, 176, 1
Gandhi, P., et al. 2006, A&A, 457, 393
Gebhardt, K., et al. 2000, ApJ, 539, L13
Gilli, R., et al. 2003, ApJ, 592, 721
Gilli, R., Comastri, A., & Hasinger, G. 2007, A&A, 463, 79
Gilli, R., et al. 2005, A&A, 430, 811
Granato, G. L., De Zotti, G., Silva, L., Bressan, A., & Danese, L. 2004, ApJ, 600, 580
Hasinger, G., Miyaji, T., & Schmidt, M. 2005, A&A, 441, 417
Hasinger, G., et al. 2007, ApJS, 172, 29
Jansen, F., et al. 2001, A&A, 365, L1
Kodama, T., et al. 2004, MNRAS, 350, 1005
La Franca, F., et al. 2005, ApJ, 635, 864
Landy, S. D., & Szalay, A. S. 1993, ApJ, 412, 64
Lawrence, A., et al. 2007, MNRAS, 379, 1599
Marconi, A., Risaliti, G., Gilli, R., Hunt, L. K., Maiolino, R., & Salvati, M. 2004, MNRAS, 351, 169
Mortier, A. M. J., et al. 2005, MNRAS, 363, 563
Peebles, P. J. E. 1980, The Large Scale Structure of the Universe (Princeton: Princeton Univ. Press)

Puccetti, S., et al. 2006, A&A, 457, 501

Martínez-Sansigre, A., et al. 2007, MNRAS, 379, L6

Mateos, S., Barcons, X., Carrera, F. J., Page, M. J., Ceballos, M. T., Hasinger, G., & Fabian, A. C. 2007, A&A, 473, 105

Miyaji, T., et al. 2007, ApJS, 172, 396

Morokuma, T., et al. 2008, ApJ, 676, 121

Mullis, C. R., Henry, J. P., Gioia, I. M., Böhringer, H., Briel, U. G., Voges, W., & Huchra, J. P. 2004, ApJ, 617, 192

Ouchi, M., et al. 2008, ApJS, 176, 301

Paolillo, M., Schreier, E. J., Giacconi, R., Koekemoer, A. M., & Grogin, N. A. 2004, ApJ, 611, 93

Saito, T., Shimasaku, K., Okamura, S., Ouchi, M., Akiyama, M., Yoshida, M., & Ueda, Y. 2008, ApJ, 675, 1076

Scoville, N., et al. 2007, ApJS, 172, 1

Setti, G., & Woltjer, L. 1989, A&A, 224, L21

Simpson, C., et al. 2006, MNRAS, 372, 741

Strüder, L., et al. 2001, A&A, 365, L18

Turner, M. J. L., et al. 2001, A&A, 365, L27

Ueda, Y., Akiyama, M., Ohta, K., & Miyaji, T. 2003, ApJ, 598, 886

Ueda, Y., et al. 1999, ApJ, 518, 656

Vikhlinin, A., & Forman, W. 1995, ApJ, 455, L109

Watson, M. G., Roberts, T. P., Akiyama, M., & Ueda, Y. 2005, A&A, 437, 899

Watson, M. G., et al. 2008, A&A, submitted (arXiv: 0807.1067)

Wolf, C., Wisotzki, L., Borch, A., Dye, S., Kleinheinrich, M., & Meisenheimer, K. 2003, A&A, 408, 499

Yang, Y., Mushotzky, R. F., Barger, A. J., & Cowie, L. L. 2006, ApJ, 645, 68

Yang, Y., Mushotzky, R. F., Barger, A. J., Cowie, L. L., Sanders, D. B., & Steffen, A. T. 2003, ApJ, 585, L85